Chem Soc Rev

# The physical chemistry and materials science behind sinter-resistant catalysts



| | |
|---|---|
| Journal: | *Chemical Society Reviews* |
| Manuscript ID | CS-SYN-09-2017-000650.R2 |
| Article Type: | Tutorial Review |
| Date Submitted by the Author: | 25-Apr-2018 |





| | |
|---|---|
| Complete List of Authors: | Dai, Yunqian; Southeast University, School of Chemistry and Chemical Engineering<br>Lu, Ping; Long Island University, Department of Chemistry and Biochemistry<br>Cao, Zhenming; Georgia Institute of Technology, ; Xiamen University,<br>Campbell, Charles; University of Washington, Department of Chemistry<br>Xia, Younan; Georgia Institute of Technology, The Wallace H. Coulter Department of Biomedical Engineering |

*MS #CS-SYN-09-2017-000650.R1*

# The physical chemistry and materials science behind sinter-resistant catalysts

Yunqian Dai,[a] Ping Lu,[b] Zhenming Cao,[b] Charles T. Campbell,[c] and Younan Xia[*b, d]

[a] School of Chemistry and Chemical Engineering, Southeast University, Nanjing, Jiangsu 211189, P. R. China

[b] The Wallace H. Coulter Department of Biomedical Engineering, Georgia Institute of Technology and Emory University, Atlanta, Georgia 30332, United States

[c] Department of Chemistry, University of Washington, Seattle, Washington 98195, United States

[d] School of Chemistry and Biochemistry, School of Chemical and Biomolecular Engineering, Georgia Institute of Technology, Atlanta, Georgia 30332, United States

Email: younan.xia@bme.gatech.edu

## TOC

This tutorial review highlights recent progress in understanding the physical chemistry and materials science for developing sinter-resistant catalytic systems.

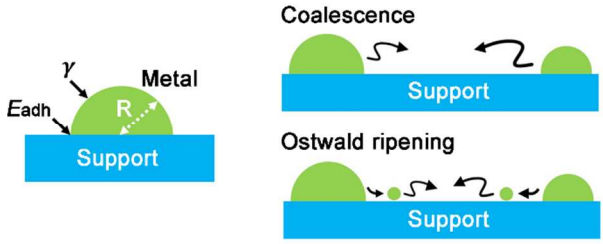

## Abstract

Catalyst sintering, the loss of catalytic activity and/or selectivity at high reaction temperatures, is a major concern and grand challenge in the general area of heterogeneous catalysis. Although all heterogeneous catalysts are inevitably subjected to sintering during their operation, the immediate and drastic consequences can be mitigated by carefully engineering the catalytic particles and their interactions with the supports. In this tutorial review, we highlight recent progress in understanding the physical chemistry and materials science involved in sintering, including the discussion of advanced techniques, such as *in situ* microscopy and spectroscopy, for investigating the sintering process and its rate. We also discuss strategies for the design and rational fabrication of sinter-resistant catalysts. Finally, we showcase recent success in improving the thermal stability and thus sinter resistance of supported catalytic systems.


**Keywords:** heterogeneous catalyst, sinter resistance, thermal stability, metal nanoparticles, oxides

**Key learning points**

1. Key obstacles to the development of sinter-resistant catalytic systems
2. Thermodynamic and kinetic aspects in the sintering of supported metal nanoparticles
3. New insights into the sintering mechanisms as elucidated through advanced analytic tools
4. Major strategies for enhancing the thermal stability of a catalytic system involving supported metal nanoparticles
5. Recent success and future directions towards the development of sinter-resistant catalysts

## 1. Introduction

Supported metal nanoparticles are widely used as hetergeneous catalysts in an array of applications, as exemplified by catalytic converters for enviromental protection and fuel cells for clean energy technology. The performance of such a catalytic system has a strong dependence on the size of the metal nanoparticles, as this parameter directly impacts the specific surface area (Fig. 1A) and the fractions of different types of atoms on the surface (Fig. 1B),[1] as well as the strength of interaction with the support. As a result, the mass activity (*i.e.*, catalytic rate per gram of metal) of such a catalyst typically shows a drastic change at about 7 nm in diameter for the metal nanoparticles involved.[2, 3] When metal nanoparticles are reduced in size, the increase in proportion for atoms sitting at the corner and edge sites can also enhance the specific activity (*i.e.*, rate per surface metal atom) because of their low coordination numbers. Taken together, it is not difficult to understand why Au nanoparticles are highly active towards a set of catalytic reactions when their sizes are kept at 3 nm or below, but they are essentially inactive at 6 nm and above.[2]

In many catalytic reactions or processes that involve high temperatures (typically, greater than 300 $^{o}$C), however, the metal nanoparticles undergo sintering (growth into larger particles) and thus lose specific surface area. Sintering can be broadly defined as the loss of metal surface area due to thermal stress rather than surface poisoning. As illustrated in Fig. 2A, sintering can follow two different modes: intra-particle and inter-particle. During intra-particle sintering, atoms rearrange on the surface of a nanoparticle, causing shape reconstruction and changes to the proportions of different types of surface atoms. For inter-particle sintering, it typically involves unbalanced transport or exchange of atoms among different particles, as well as coalescence (Smoluchowski ripening or agglomeration) of the particles into larger ones. In the following discussion, "sintering" simply means "inter-particle sintering" unless specified otherwise. Sintering will cause significant deterioration to the performance of a catalytic system because of *i*) the decrease in specific surface area and thus the number of active sites; *ii*) the reduction in contribution from low-coordination atoms at edges and corners; and *iii*) the variation of electronic structure, which can lead to different adsorption and/or desorption energy barriers for the reaction intermediates and thus different reaction pathways.[4] It should be noted that, besides sintering, several other factors can also cause catalyst deactivation, such as poisoning, coking, leaching, and strong metal-support interaction (SMSI).[5, 6] These causes of catalyst deactivation

are not independent from each other, and they strongly depend on the reaction environment (*e.g.*, CO, $O_2$, or $H_2O$ vapor). In some cases, the sintered catalyst could be reactivated through re-dispersion, the reverse of sintering, in the presence of $O_2$ and/or $Cl_2$. In this process, the sintered metal nanoparticles sometimes form volatile metal oxide or chloride complexes, which are, in turn, reduced to generate small metal nanoparticles.[5, 7] However, it is almost impossible to fully recover the original catalytic activity. As a result, precious metals, particularly those for automotive emission control, have to be loaded in large excess to ensure the targeted lifetime on-stream. For instance, in automotive catalysts, every kilogram of the monolith could contain as much as 2.2 grams of precious metals (Pt, Pd, and Rh) in order to achieve a lifetime of roughly 10 years.[7] Because of sintering, many promising catalytic systems never advance to practical use.

Although the undesirable sintering phenomenon is typically involved during the operation of a catalyst at elevated temperatures, it can also occur at a relatively low temperature or even during the preparation of a catalyst. A notable example can be found in the Pt/C catalyst commonly used at 80 $^{o}$C for the proton-exchange membrane fuel cells.[8] In addition, during an exothermic reaction, the actual temperature at the catalyst's surface can markedly exceed the temperature of the surrounding, greatly accelerating the sintering kinetics.[9] During the oxidation of CO on Pt, for example, the energy released is about $4.8\times10^{-19}$ J per $CO_2$ molecule produced, which is more than enough to cause small metal nanoparticles to migrate and/or melt.[10] As a result, a catalytic system can also dramatically lose activity because of sintering even during operation at a relatively low temperature.

Despite the long history of and major advancement in heterogeneous catalysis, it remains a daunting challenge to develop thermally-stable catalytic systems. While all nanoparticle-based catalysts inevitably sinter over time, the immediate and drastic consequences can be mitigated by uncovering the mechanistic details of sintering and the critical parameters that can be optimized to slow down or suppress the sintering process. The last decade has witnessed remarkable progress in developing a deep understanding and good control of sintering for the development of catalysts with greatly enhanced thermal stability. It is clear that some of the adverse impacts caused by sintering can be mitigated or even circumvented by carefully designing the catalyst in terms of composition and structure.

In this tutorial review, we concentrate on the recent progress in sinter-resistant catalysts with a focus on the current mechanistic understanding in terms of physical chemistry and

experimental controls related to materials science. We begin with a brief introduction to the fundamentals of catalyst sintering in the context of thermodynamic and kinetic perspectives. We then discuss a set of advanced tools and techniques for monitoring the sintering process, and further illustrate the key strategies for the development of sinter-resist catalytic systems. Finally, we highlight several recent examples in achieving thermally-stable catalysts. We conclude this article with personal perspectives on optimizing the sinter-resistance capability of active metal nanoparticles without compromising their catalytic activity.

## 2. Fundamentals of catalyst sintering

A deep understanding of the sintering mechanisms and pathways is crucial to the rational design and fabrication of sinter-resistant catalysts. To this end, physical chemistry has played a central role in quantifying the thermodynamic and kinetic factors involved in the sintering of supported metal nanoparticles, including elucidation of the driving force(s), identification of the pathway(s), and determination of the parameters for experimenting with sintering.

### 2.1 The driving force for sintering

From the standpoint of thermodynamics, the sintering of nanoparticles in a catalyst is driven by the forces that reduce the total surface free energy of the entire system. Unsupported solid particles are driven to evolve toward the equilibrium shape defined by the Wulff construction, and when sitting on a support, this is modified by the adhesion energy ($E_{adh}$) as defined through the Winterbottom construction.[11]

The chemical potential ($\mu$, or partial molar Gibb's free energy) of a surface atom on a supported metal nanoparticle is a direct measure of how unstable the atom is with respect to the bulk metal (or large-particle limit), and thus the thermodynamic driving force for sintering.[2, 12, 13] When the chemical potential of the atom on a metal nanoparticle is increased, it will experience a greater thermodynamic driven force towards sintering, and thus acceleration of sintering. For a large hemispherical particle of $R$ in radius attached to a support with an adhesion energy of $E_{adh}$ at the particle/support interface (Fig. 2B), the chemical potential was proven to be[12]

$$\mu(\mathrm{R}) = (3\gamma_{\mathrm{m}} - E_{adh})(V_{\mathrm{m}}/R) \qquad (1)$$

where $\gamma_{\mathrm{m}}$ is the surface energy of the bulk material, $V_{\mathrm{m}}$ is its molar volume, and the bulk material (particle with infinite size) is taken as the reference state of zero chemical potential. Previously,

the Gibbs-Thomson relation ($\mu$(R)=2$\gamma_m V_m/R$) had been used to estimate $\mu$(R) by neglecting the term of adhesion energy.

Extensive experimental measurements of $\mu$(R) for late transition metal nanoparticles on oxide supports have shown that the chemical potential increases faster with decreasing particle size than predicted by Eq. (1), when they are smaller than 6 nm in average diameter. A much more accurate fit to these data was given by:[13]

$$\mu(R_{\text{eff}})=(3\gamma_m-E_{\text{adh}})[1+D_0/(2R_{\text{eff}})](V_m/R_{\text{eff}}) \quad (2)$$

where $[1+D_0/(2R_{eff})]$ is an empirical correction that accounts for the fact that $3\gamma_m-E_{adh}$ increases with decreasing particle size below 6 nm in diameter. The data were well fitted with $D_0$ = 1.5 nm.[13] The increase in $\gamma_m$ is due to the increase in the fraction of coordinatively-unsaturated metal atoms (like those at steps and kinks) as size decreases.[13-15] The $R$ is replaced with $R_{eff}$ in Eq. (2) because the shape and diameter of the particle are generally unknown. When the average volume is known, $R_{eff}$ is defined as the radius of a hemispherical particle of that volume. Lowering the free energy of the nanoparticles (or $\mu$) by increasing the strength of adhesion between the metal and the support can effectively mitigate sintering.[16]

### 2.2 Pathways for sintering: Coalescence *vs.* Ostwald ripening

Reducing the chemical potential of the surface atoms serves as a universal thermodynamic driving force for sintering. The actual process of sintering involves transport of matter along a definite path, which can be used to define the pathway or mode of sintering. In general, the sintering of a catalyst can occur through two different pathways: *i*) coalescence and *ii*) Ostwald ripening.[2] For the coalescence mechanism, two or more metal nanoparticles migrate across the surface of a support through Brownian-like motion until they meet and merge into a larger particle (Fig. 3A). The diffusion of particles is faster when metal-support interactions are weaker, and their coalescence is faster when particles are in closer proximity. For the Ostwald ripening mechanism (Fig. 3B), individual metal atoms (*i.e.*, "monomers") leave the surface of one nanoparticle to join another nanoparticle *via* surface diffusion across the support or transport through the vapor (or solution) phase.[3] In the case of supported catalysts, the metal atoms commonly transfer across the support surface rather than through the vapor phase, unless volatile compounds are involved.[17] Transferring of metal atoms through the vapor phase tends to cause mass loss for the active component. Since the chemical potential is lower in larger particles, the

larger particles are more favored for growth at the expense of smaller ones, which decrease in size and eventually disappear (Fig. 3B). The Ostwald ripening mechanism is usually responsible for the sintering of metal nanoparticles that are well spaced apart on a support.

Differentiation of these two mechanisms of sintreing is not an easy task as the sintering may be dominanted by both of them either simultaneously or alternatively. The particle size distribution (PSD) has been claimed to serve as an indicator to identify the explicit sintering pathway.[18] However, at sizes below 6–10 nm in diameter, it is difficult to use the shape of the size distribution curve to determine the sintering pathway.[15] Coalascence always gives rise to a decrease in particle number density whereas Ostwald ripening at the early stage is characterized by a fixed particle number density,[9] albeit with a broad PSD, the smallest particles may disappear before one sees any measureable increase in size for the larger particles. Thus, comparing PSDs before and after sintering is not so reliable for assessing the mechanism, and the most reliable way is to monitor the fate of the particles involved using microscopy during the course of sintering. As demonstrated by experimental observations, the sintering pathway is also dependent on the particle size. For example, $Au_{561\pm13}$ and $Au_{923\pm20}$ clusters were found to undergo Ostwald ripening, whereas $Au_{2057\pm45}$ sintered through coalescence only, under the same conditions used for catalytic CO oxidation at 250 $^{o}$C.[19] The apperance of different sintering pathways was attributed to the fact that the energy liberated from CO oxidation varied as a function of cluster size. In the case of large clusters, the gained energy was not adequate to drive atoms to detach from the cluster for Ostwald ripening, and thereby only coalescence was possbile.[19]

**2.3 Kinetic aspects of sintering**

An understanding of sintering kinetics allows one to obtain the key parameters that determine the rate of sintering and thereby predict the long-term stability of a catalyst based on short-term measurements. No matter which mechanism is involved, the rate of sintering has a strong correlation with temperature. This is easy to understand because both mechanisms require the breaking of bonds between metal atoms and between metal atoms and the support surface. Increase of temperature can activate the sintering process by accelerating the diffusion of both metal atoms and nanoparticles, and the detachment of metal monomers from particles. The temperature at which sintering starts to occur can be roughly estimated using the semi-empirical

Hüttig and Tamman temperatures:[20]

$$T_{\text{Hüttig}} = 0.3T_{\text{melting}} \quad (3)$$

$$T_{\text{Tamman}} = 0.5T_{\text{melting}} \quad (4)$$

where the temperatures are absolute temperatures. At the Hüttig temperature ($T_{\text{Hüttig}}$), the atoms at surface start to exhibit mobility. At the Tamman temperature ($T_{\text{Tamman}}$), the atoms from the bulk become mobile and bulk diffusion is observable. The values of $T_{\text{Tamman}}$ for the precious metals, calculated from melting points,[21] can be found in Fig. 4. This method neglects the metal/support adhesion energy, which dramatically affects the sintering kinetics (see below). In considering the sintering temperature, it is worth emphasizing that the melting point of a metal nanoparticle is much lower than the bulk material,[22] as reflected in Eq. (5):

$$\frac{T_{\text{m}}(R)}{T_{\text{m}}(0)} = 1 - \frac{2}{\rho_s L}\left\{\gamma_s - \gamma_l\left(\frac{\rho_s}{\rho_l}\right)^{2/3}\right\}\frac{1}{R_s} \quad (5)$$

where $T_{\text{m}}(R)$ is the melting point of a particle with radius $R$; $T_{\text{m}}(0)$ is the melting point of the bulk material; $\rho_{\text{s}}$ and $\rho_l$ are the densities of the solid and liquid phases, respectively; $\gamma_{\text{s}}$ and $\gamma_l$ are the surface free energies of the solid and liquid phases, respectively; and $L$ is the molar heat of fusion. Due to this melting-point depression phenomenon, the melting points of nanoparticles could be significantly lower than the bulk material. For instance, the melting point of 2-nm Au nanoparticles is only about 327 $^{\text{o}}$C,[21] in sharp contrast to the melting point of 1065 $^{\text{o}}$C for bulk Au. Moreover, for particles with given sizes, the rate of sintering tends to increase exponentially with temperature.[5] At a fixed temperature, the rate of sintering slows down dramatically as particles grow into sizes beyond 6 nm in diameter because their chemical potentials decrease to nearly the large-size limit by the time they reach 6 nm, thus the thermodynamic driving force drops to near zero.[15]

The rate of sintering is also dependent on the surrounding atmosphere. Commonly, supported metal nanoparticles sinter more rapidly under an oxidizing atmosphere (*e.g.*, air and $O_2$) than in vacuum, while the sintering process becomes much slower under a reducing or inert atmosphere (*e.g.*, $H_2$, He, and Ar).[5, 23] In addition, the kinetics of sintering are also dependent on several other factors such as the size, shape, and composition of the initial nanoparticles; catalyst loading and dispersion; and composition and structure of the support.[5]

The rate of sintering has a strong correlation with the chemical potential of atoms on the surface. In general, the greater is the thermodynamic driving force, the faster the sintering will be.

When Ostwald ripening is the dominant mechanism, the radius ($R$) of a given particle at any time changes at a rate that depends dramatically on the chemical potential of its surface atom, $\mu(R)$. When the detachment of monomers from the particle is rate-determining, the rate is given by:[13, 15]

$$\frac{dR}{dt} = \frac{K}{R}\left(\exp\left[\frac{-E_{tot}}{kT}\right]\right)\left(\exp\left[\frac{(\mu(R^*)}{kT}\right] - \exp\left[\frac{(\mu(R)}{kT}\right]\right) \qquad (6)$$

where $K$ and $E_{tot}$ are system-dependent constants and $R^*$ is the equilibrium radius for the concentration of diffusing monomers at that time. The concentration is determined by the size distribution of all particles in the catalyst. Particles smaller than $R^*$ get smaller (*i.e.*, $dR/dt$ is negative) while those larger than $R^*$ grow in size. Here $E_{tot}$ is the metal's bulk sublimation enthalpy minus the adsorption energy of a monomer on the support plus the diffusion activation energy of a metal atom on the support, $k$ is Boltzmann's constant, and $K$ is the pre-factor for a surface atom to detach from a large particle and become a monomer on the support times a geometric constant. If sintering is dominated by coalescence, the rate is also nearly proportional to $e^{\mu(R)/kT}$. The best current way to estimate $\mu(R)$ is Eq. (2), which includes the metal/support adhesion energy ($E_{adh}$), but that has not yet been used together with Eq. (6), which has only been applied using estimates for $\mu(R)$ that depend only on the metal itself, like the Gibbs-Thompson equation or bond-additivity.[15] This kinetic model has been used to predict long-term stability based on short-term measurements.[13, 15] The use of Eq. (6) was improved by Datye's group by improving the way $R^*$ is calculated.[24] Since $E_{adh}$ has never been included when estimating $\mu(R)$ for applications of Eq. (6), there is room for considerable improvement in its use. Increasing $E_{adh}$ by changing the support is known to dramatically decrease the rate of sintering,[16] as is obvious from combining Eq. (2) with Eq. (6).

## 3. Techniques for studying the sintering process

One of the major hurdles that limit the development of sinter-resistant catalysts is to elucidate how sintering occurs, particularly at the atomic level. The sintering process has been most commonly investigated by *ex situ* methods after going through treatment at a certain temperature or a realistic catalytic reaction for a given period of time. The study involves comparison of the ensemble averages, PSDs, shapes, and sometimes compositions. Because sintering is such a dynamic process, it is hard to capture all the mechanistic details through *ex*

*situ* investigation. With the rapid development of *in situ* methods, especially with the help of advanced electron microscopy tools, sintering can now be tracked and analyzed in real time and with atomic resolution. These advanced techniques are summarized and compared in Table 1.[2-4, 9, 13, 14, 25, 26]

### 3.1 *In situ* electron microscopy

Electron microscopy can be used to directly provide information with regard to individual particles in a catalyst. Advances in *in situ* transmission electron microscopy (TEM), in particular, has enabled the analysis of sintering pathways and kinetics in a selected area by directly tracking changes to the size, shape, structure, composition (when combined with spectroscopy analysis), lattice spacing in real time.[25] *In situ* TEM has become one of the most powerful tools for identifying the sintering pathway as it can record "atomic movies" of the supported metal nanoparticles in real time and reveal the most mobile atoms responsible for sintering at the initial stage. Real-time observation of metal nanoparticles with well-defined shapes is also instrumental to the identification of thermally unstable facets that should be reduced to the lowest possible proportion or selectively capped.[27]

The sintering of a catalyst is often accelerated in the presence of an oxidative gas such as $O_2$. However, if the gas converts the metal to its oxide that wets the support, the gas can be used to re-disperse the catalyst. The role played by a gas can vary from system to system under realistic conditions and needs to be precisely determined.[28] To this end, environmental TEM (ETEM) capable of simulating a particular gas environment (*e.g.*, CO, $O_2$, $H_2O$ vapor, or air) offers a versatile tool for probing nanoscale/atomic scale catalytic behaviors in a selected chemical environment and at an elevated temperature.[8, 25] In this case, the specimen holder is integrated with an environmental cell, in which the gas (up to certain pressures) is confined between two membranes that are thin enough for electrons to penetrate through. Such a setup is often referred to as a nanoreactor. This is an area of critical importance for catalysis although it is still in the early stage of development in terms of systematic investigation.[25] In a recent study, the size evolution of Pt nanoparticles dispersed on a planar amorphous $Al_2O_3$ support was monitored and analyzed using ETEM by subjecting the sample to 10 mbar synthetic air composed of 21% $O_2$ and 79% $N_2$ at 650 $^oC$ (Fig. 5A).[29] The particles with large initial diameters grew bigger over the course of time while particles with small initial diameters shrank and eventually disappeared. On

the other hand, short-term *in situ* study of nanoparticles subjected to a high temperature can help predict the long-term sintering behavior of the catalyst. In one study, the sintering of Ni nanoparticles supported on $MgAl_2O_4$ was accelerated by heating the sample to 750 $^oC$ under conditions relevant to steam reforming.[30] The activation energy was then derived by analyzing the size change of a limited number of nanoparticles to model the long-term sintering process.

In addtion to size evolution, the dynamics of structural evolution has been investigated at the atomic level. In a recent study, the dynamics of Pt nanoparticles supported on carbon nanotubes (CNTs) was analyzed using *in situ* aberration-corrected ETEM under a fuel cell relevant gas at 100 $^oC$.[8] In comparison with the case of $H_2O$, $O_2$ promoted the migration of Pt nanoparticle on a carbon surface. Atomically, the coalescence featured reorientation of the particles towards lattice matching, a process driven by orientation-dependent van der Waals forces (Fig. 5B).[8] Using a novel sealed gas cell sample holder, the dynamics of structural transformation of Pd@$CeO_2$ core-shell nanoparticles, which exhibited striking activity towards methane combustion while resisting against sintering, could be observed inside ETEM by *in situ* calcination treatment up to 650 $^oC$ under 150 torr of pure $O_2$.[31] The *in situ* data offers an insightful explanation about the formation of the atomic-scale species and the very small entities observed in samples after *ex situ* calcination at 800 $^oC$. The original clusters of 2–3 nm Pd@$CeO_2$ nanoparticles evolved into a final mixture of 5–20 nm particles and a new structure containing Ce, Pd, Si, and O in a very highly dispersed form. The coarse particles of $CeO_2$ and Pd were supposed to show the conventional catalytic behavior while the new structure seemed to be responsible for the unique catalytic properties and it might contain ionic Pd bonded to $CeO_2$.

Scanning tunneling microscopy (STM) is another powerful technique for atomic-resolution tracking of mobile nanoscopic objects. Researchers could monitor the disturbed electronic state of a metal atom coordinated to organic species and identify the key processes of sintering that underlies gas-induced mass transport.[4] It is of critical importance to resolve how the adsorbed species impact the kinetics of sintering, and how the information can be used to deduce the effects of coordination moieties (*e.g.*, H, OH, and CO) that play pivotal roles in determining the diffusion or anchoring of atomic species on the surface. For example, the sintering dynamics of Pd atoms on the $Fe_3O_4$ (001) surface were investigated under $5\times10^{-10}$ mbar of CO.[28] The CO moieties induced coalescence of atomic Pd-CO species at the initial stage, followed by further coarsening *via* cluster diffusion and coalescence. While the CO species induced metal adatom

mobility in this $Pd/Fe_3O_4$ model catalyst, the surface OH group showed an opposite effect and could help anchor Pd atoms.

### 3.2 *In situ* spectroscopic techniques

Spectroscopic techniques are able to statistically account for the physicochemical changes to a catalyst, including the variation of chemical state or oxidation state of the metal species during sintering. Previous studies suggest that the formation of volatile metal-oxygen species in an oxidizing environment is likely responsible for accelerating the sintering rate of supported metal nanoparticles at elevated temperatures.[5] This speculation was confirmed recently through *in situ* high-pressure X-ray photoelectron spectroscopy (HP-XPS) study of Pt nanoparticles on $SiO_2$.[23] This work offers a molecular-level understanding of the nature of sintering during the operation of a catalyst. When probed under oxidizing condition (0.5 Torr $O_2$), HP-XPS revealed a drastic decrease in the Pt *4f* signal at temperatures above 450 $^oC$. In contrast, the Pt *4f* signal remained the same at temperatures up to 600 $^oC$ under reducing conditions (0.5 Torr $H_2$) (Fig. 6A). The attenuation in Pt *4f* signal under $O_2$ was caused by the formation of volatile $PtO_x$ species (*e.g.*, $PtO_2$ and PtO).

In addition to these direct *in situ* characterization techniques, indirect *in situ* methods can also be used to scrutinize nanoparticle sintering, sometimes, at a much higher resolution. For example, indirect nanoplasmonic sensing (INPS) has been utilized to measure sintering kinetics with a temporal resolution in the sub-second range under different gas environments, including $O_2$, $H_2$ and $NO_2$.[9, 26] INPS measures the optical transmission spectra through an Au nanoplasmonic sensor chip (Fig. 6B).[26] The optical response of INPS, or the centroid shift of localized surface plasmon resonance (LSPR) peak, showed an unambiguous linear correlation with the density of catalyst particles. Sintering kinetics was then derived by translating the density of catalytic particles into a size distribution and average particle diameter. Based on this method, this work monitored the dependence of sintering rate of a $Pt/SiO_2$ model catalyst on the $O_2$ concentration in the Ar carrier gas.[26] The sintering rate of Pt nanoparticles strongly depended on the $O_2$ concentration in the 0.05–0.5 % range. The rate was accelerated upon increasing the $O_2$ partial pressure (Fig. 6C). These observations highlight the importance of adsorbate-modulated nanoparticle surface energies to the occurrence of catalyst sintering and re-dispersion.[26] Adsorbates can also bind to the diffusing metal monomers, decreasing $E_{tot}$ in Eq.

(6).

### 3.3 Calorimetric measurements

Adsorption microcalorimetry directly measures the bonding energy (adsorption energy) of metal atoms to supported metal nanoparticles.[2, 3, 12-14, 16] Based on such measurements, the chemical potential of a metal nanoparticle can be estimated by the difference in magnitude between the bulk heat of sublimation of the metal and its differential heat of adsorption on particles of that size while neglecting the difference in entropy. The resulting curves, like those in Fig. 7A, clearly illustrate the thermodynamic driven force of sintering at the atomic scale. If a metal atom is less stable on a particle of a certain size than in the bulk, it prefers to move to a larger particle to make it more stable, triggering sintering, that is, moving to a site lower in energy (to the right on each of the curves) until it reaches the minimum, or zero.[3]

The inclusion of accurate size dependence of particle energies in kinetic models is crucial to accuracy in predicting the long-term sintering behavior of catalytic nanoparticles. As shown in Fig. 7B, Eq. (2) provides an accurate estimate of chemical potential, and thus should reproduce sintering kinetics *via* Eq. (6). Crucial to Eq. (1) and Eq. (2) is the knowledge of $E_{adh}$. We have recently discovered predictive correlations between the $E_{adh}$ for metal/oxide interfaces and the oxophilicity of the metal and of the oxide surface, and the density of oxygen atoms on the oxide surface.[13]

## 4. Key strategies for achieving sinter resistance

The fundamental knowledge of how sintering occurs and how its kinetics depend on system parameters has been translated to the development of strategies for improving the thermal stability of catalytic systems based on metal nanoparticles with different sizes, shapes, and compositions on various types of supports. In the following subsections, we discuss how these strategies have been explored to suppress sintering through thermodynamic and/or kinetic controls.

### 4.1 Controlling the uniformity of the metal nanoparticles

Sintering can be mitigated by optimizing the properties of the metal nanoparticles, including the uniformity in terms of size, shape (*i.e.*, the type of facet or surface structure), structure, and composition. Ostwald ripening can be mechanistically described as large particles growing at the

expense of smaller ones as driven by the difference in chemical potential. Mass transport between the growing and shrinking particles is governed by detachment of species from smaller particles with higher chemical potentials, which then attach to larger particles with lower chemical potentials. As such, this process can be suppressed using nanoparticles with essentially the same size to eliminate the difference in chemical potential. Taking the size-selected $Pt_{68}$ clusters on $SiO_2$ support as an example, Ostwald ripening could be suppressed even under the sinter-promoting condition involving hydrogen oxidation and a high surface coverage for the clusters (Fig. 8A and B).[9] While the size-selected metal clusters have good uniformity in size, their geometric shapes and therefore the chemical potentials of surface atoms tend to be different. Such subtle differences could account for the occurrence of sintering eventually observed in the size-selected Au clusters.[19] Additionally, the uniformity in size is also instrumental in reducing the reaction-induced destabilisation of small particles.[10] Avoiding broad size distribution at the starting point of a sintering process could greatly improve the thermal stability.

The sinter-resistance of a catalyst can also be enhanced by tailoring the shape of metal nanoparticles. Nanoparticles with an equilibrium shape are more favored for slowing down the sintering kinetics. For metal nanoparticles featuring sharp corners/edges and high-index facets, their shapes are far from equilibrium, with a high density of low-coordination atoms on the surface. These features can endow the atoms with sufficiently high chemical potentials to leave their initial locations and migrate to the more stable sites.[27] In general, particles approach their equilibrium shape before inter-particle sintering occurs as metal atoms can diffuse across the surface of a particle more easily than being detached from the particle. Partially capping the active sites with atoms having a lower chemical potential can help preserve both the size and shape of particles at elevated temperatures by slowing down intra-particle sintering. For instance, the thermal stability of Pd nanocubes could be significantly enhanced by depositing Rh atoms at the corners and edges to generate Pd-Rh core-frame nanocubes. The core-frame nanocubes were able to maintain their size and cubic shape after heating at 500 $^{o}$C for 1 h (Fig. 8C and D), in contrast to the Pd nanocubes that evolved into a spherical shape and most of the adjacent particles started to melt together upon heating to 500 $^{o}$C for only 3 min.[32] This example demonstrates that elimination of those metal species with higher energy is indeed effective in slowing down the sintering kinetics.

The composition of metal nanoparticles also has a great impact on the thermal stability.

Incorporating a metal with a higher sublimation energy into catalytic nanoparticles can enhance their thermal stability to a greater temperature. When the thermal energy is not sufficient to activate the migration of the adatoms, sintering will be mitigated. For instance, the thermal stability of Pt nanoparticles could be greatly increased when it was alloyed with Rh.[10] Similar improvement in thermal stability was also observed in other bimetallic nanoparticles with different compositions, including AuIr, AuAg, and AuCu, as the existence of new metal oxide phase (*e. g.*, $IrO_2$, AgO, and CuO) provides stronger $E_{adh}$ and thus a reduced chemical potential.[33] Recent work has demonstrated that the addition of Ir atoms made the resultant AuIr bimetallic nanoparticles intrinsically lower in free energy. In the form of an alloy, these nanoparticles could resist sintering when uniformly dispersed on the support with the nearest neighbor distance being long enough to avoid sintering by slowing down the mass transfer of metal atoms (Fig. 8E and F).[33] In this system, however, it was the Ir rather than $IrO_2$ that increased the $E_{adh}$ for anchoring the catalytic particles to the support more strongly, particularly for the anatase-based support.

**4.2 Enhancement of chemical bonding at the metal-support interface**

A stronger chemical bonding between metal nanoparticles and their support can help retard the sintering process. The detachment of metal atoms from a nanoparticle is determined by the number of metal-metal bonds and the strength of metal-oxide interfacial chemical bonding. Strong adhesion of metal nanoparticles (Ag, Ir, and other late transition metals) to supports (including $CeO_2$, MgO, and perovskites) is responsible for their resistance to sintering. Chemical bonding at the interface is both metal- and support-dependent. For a given metal, the $E_{adh}$ differs among oxides, and even between different types of facets on the same oxide, in the increasing order of MgO(100) ≈ $TiO_2$(110) < α-$Al_2O_3$(0001) < $CeO_2$(111) ≈ $Fe_3O_4$(111),[12] which can be correlated with the decreasing oxophilicity of the oxide and increasing density of surface O atoms.[13] Under ultrahigh vacuum (UHV) condition, the presence of oxygen vacancies in the oxide surface often increases $E_{adh}$, but surface hydroxyl groups appear to decrease $E_{adh}$.[3] For a given oxide, the $E_{adh}$ of different metals increases linearly with increasing heat of formation of the most stable oxide of the metal per mole of metal (a measure of metal oxophilicity).[12] Under realistic conditions, environmental factors, such as gas atmosphere, can alter the adhesion energy between metal and support and thus the resistance to sintering under these conditions.

The strong chemical bonding at the metal-support interface can even be used to stabilize

(usually) very mobile single atoms on a support through the enhanced metal-oxide bonding. In one example, the charge transfer from Pt atoms to the $FeO_x$ surface was determined to be responsible for their remarkable thermal stability and high activity towards CO oxidation. According to density functional theory (DFT) calculations, the most stable sites for single Pt atoms on the support were the three-fold hollow sites on the $O_3$-terminated surface, where each Pt atom was coordinated to three surface oxygen atoms.[34] In another study, it was found that the strong chemical bonding was beneficial to the ability of $CeO_2$ to trap mobile Pt species and stabilize Pt single atoms in an atomically dispersed state (Fig. 9A).[35] The $CeO_2$ nanoparticles were physically mixed with Pt/La-$Al_2O_3$ and aged at 800 $^oC$ under air, the typical diesel oxidation catalyst (DOC) condition, for 10 h. Mobile $PtO_2$ was rapidly ejected from the La-$Al_2O_3$-supported Pt and immobilized on the clean surface of $CeO_2$ (Fig. 9B). After three cycles of CO oxidation going up to 300 $^oC$, the step edges on the $CeO_2$ rods were decorated with Pt atoms while the well-defined {111} facets did not show any Pt species (Fig. 9C). This site preference is consistent with DFT calculations, which suggest that the binding energy of Pt to surface steps on $CeO_2$ exceeds that of Pt to $CeO_2$ (111). Atom trapping is an attractive strategy for capturing mobile $PtO_2$ with non-volatile PdO to regenerate a Pt-Pd bimetallic catalyst for diesel oxidation with improved thermal stability.[36]

The strength of chemical bonding could be enhanced by selectively anchoring metal nanoparticles on the specific facet(s) of an oxide, as $E_{adh}$ depends sensitively on the crystal facet of the support.[3] For instance, small Pt nanoparticles (1–3 nm) on the small {111} facets of a $MgAl_2O_4$ cuboctahedral nanoparticle can survive harsh sintering condition, leading to the maintenance of high Pt dispersion, while those on {100} facets sintered under the same condition. Theoretical simulations reveal that the (111) surface favors the epitaxial growth of Pt(111) in a lattice-matched fashion, while the (100) surface repels Pt(100).[37] The small dimensions of the exposed {111} facets therefore limit the size of the attached Pt nanoparticles, contributing to the prevention of Pt sintering. Taken together, choosing a proper oxide with the desired facets exposed on the surface at a large fraction can be used to mitigate the sintering of metal nanoparticles.

### 4.3 Physical confinement

Physical confinement is the most prevalent and extensively explored strategy for improving

the thermal stability of a catalyst, at temperatures beyond its Tamman temperature. The core concept of this strategy is the encapsulation of metal nanoparticles in a porous matrix, or conformal deposition a protective layer on top of the particle (Fig. 10A).[38] In one example, it was reported that embedding Pt nanoparticles in mesoporous $TiO_2$ matrix enabled strikingly better thermal stability in *n*-hexane reforming up to 500 $^oC$, giving enhanced activity and selectivity (Fig. 10B and C).[39] In contrast to the system deposited on mesoporous $SiO_2$ ($mSiO_2$), the excellent stability of Pt nanoparticles on $TiO_2$ was a result of the strong chemical bonding at the Pt-$TiO_2$ interface. As such, it is more favorable to confine the metal nanoparticles in a matrix having strong chemical bonding at the metal-support interface.

Oxides (*e.g.*, $SiO_2$, $Al_2O_3$, $ZrO_2$, and $TiO_2$) are usually used for creating the protective layer because they are thermally stable, chemically inert, and mechanically strong. Since the materials of supports are also oxides in most cases, the nanoparticles are commonly sandwiched between two layers of different or the same oxide materials. The coating has two functions: *i*) as a physical barrier to spatially confine the metal nanoparticles from sintering, *ii*) passivating specific sites susceptible to sintering at the very beginning and thus altering the rates of atom detachment and transport on the support. The protective layer does not necessarily need to be thin but it must be highly porous. When considering this strategy, people should notice the densification of porous films at an elevated temperature, which tends to result in undesirable cracks, losing the initial function of physical confinement.[38] In another study, Pd nanoparticles were embedded in porous $CeO_2$ cocoon.[40] The resultant core-shell nanostructures were then deposited on silane-modified $Al_2O_3$. This catalytic system exhibited exceptional thermal stability and activity toward methane oxidation. The confined Pd nanoparticles did not show notable sintering even at a temperature up to 850 $^oC$, primarily due to the effective protection of the $CeO_2$ shell and the optimal dispersion on the modified $Al_2O_3$ support (Fig. 10D and E).

The improved thermal stability of a physically protected catalyst usually comes at an expense of the catalytic activity as compared to that of the pristine catalyst due to the blocking of active sites and/or the retarded mass transfer. Alternatively, partial encapsulation of the surface of metal nanoparticles can effectively slow down their sintering while keeping enough active sites exposed. For example, when Au nanoparticles supported on hydroxyapatite (HAP) were calcined in air at temperatures in the range of 200–600 $^oC$, the Au surface was gradually encapsulated by HAP, and the extent of encapsulation was determined by the temperature.[41]

Upon partial encapsulation, the Au nanoparticles could be prevented from sintering while presenting a large portion of the active sites. In another demonstration, the surface-bound organic surfactants were directly converted into carbon shells to serve as a physical barrier for impeding the sintering of metal nanoparticles.[42] After heating in $N_2$ at 500 $^oC$, for example, the olyelamine on Au surface could be carbonized to generate a conformal coating. Due to the confinement effect, Ostwald ripening was depressed when the catalyst was calcined in air for the generation of a clean surface by removing the carbonaceous coating. The clean Au nanoparticles were highly resistant to sintering, with improved sintering resistance up to 600 $^oC$.

### 4.4 Energy barrier as a kinetic bottleneck

Besides the construction of a physical barrier to prevent metal nanoparticles from sintering, energy barriers can also be applied to hinder metal nanoparticles from sintering through the surface diffusion route. A dual-oxide support consisting of size-controlled nanoscale domains of two different oxides represents a promising candidate. In such a structure (Fig. 11A), small areas of a strongly-interacting oxide support (*i.e.*, high in $E_{adh}$, for $CeO_2$ or $TiO_2$) are completely surrounded by a weakly-interacting oxide (*i.e.*, low in $E_{adh}$, for $SiO_2$ or $Al_2O_3$). Metal nanoparticles are then deposited on the strong-oxide domains in the form of one nanoparticle per domain. For the sintering of metal nanoparticles *via* surface diffusion, the metal atom or nanoparticle must move across the support to attach to or merge with other nanoparticles. The energy barrier associated with such motion is much greater on the dual-oxide support than the traditional single-oxide support (Fig. 11B). The energy barrier can act as a kinetic bottleneck to prevent the catalyst from sintering, thus enhancing its long-term stability.[14] The resistance of this kind of dual-oxide-supported catalyst against sintering has been validated using a dual-oxide support comprised of $TiO_2$-$SiO_2$.[43] This dual-oxide support was formed by substituting Ti for Si in a $SiO_2$ thin film network to form Ti or $TiO_x$ islands, followed by selective nucleation of Au clusters on the $TiO_x$ domains. Upon exposure to reaction temperatures up to 577 $^oC$, the Au clusters did not noticeable sign of sintering.

## 5. Recent examples of sinter-resistant catalysts

Developments in materials science have triggered technological innovation and industrial revolution, and have also provided good opportunities and strategies for the rational design of

novel sinter-resistant catalysts. In this section, we discuss how the key strategies can be harnessed for achieving sinter-resistant catalysts based on zero-, one-, and three-dimensional supports.

**5.1 Zero-dimensional systems based on nanoparticles**

Recent demonstrations suggested that encapsulation of metal nanoparticles in ultrathin, porous shells of oxide could largely preserve their catalytic activity while increasing the resistance against sintering. As an early example of such a synthesis, metal nanoparticles were partially embedded in the inner surface of ceramic hollow particles by employing polystyrene (PS) beads as a sacrificed template.[44] Ever since, a wide variety of wet-chemical methods have been reported for the encapsulation process, and some of them are also suitable for scale-up production. For example, a method based on the use of reverse micelles as discrete nanoreactors was reported for the synthesis and then encapsulation of $Pt/FeO_x$ nanoparticles (1.8 nm in size) in porous $SiO_2$ shells (Fig. 12A).[45] This system is of considerable interest due to the favorable metal-support interaction at the $Pt/FeO_x$ interface for enhancing the catalytic activity of Pt. During the preferential CO oxidation in $H_2$ (PROX) at 180 $^oC$, the catalytic activity of the $Pt/FeO_x@SiO_2$ nanoparticles could be maintained at a high level for up to 41 h (Fig. 12B). In a control experiment with $Pt/FeO_x$ nanoparticles only, the catalytic activity dropped significantly after 24 h. At a lower temperature of 100 $^oC$, the catalytic activity of the $Pt/FeO_x@SiO_2$ nanoparticles could be retained up to 84 h, but the $Pt/FeO_x$ system initially exhibited a higher activity toward PROX at 100 $^oC$ due to better accessibility of the catalyst. After this harsh reaction, the $Pt/FeO_x$ components were stable in the $SiO_2$ shells up to 84 h at 100 $^oC$ (Fig. 12C).

Selective passivation of specific sites where metal atoms have high chemical potentials, like edges and corners, could slow down the kinetics of atom migration across the surface. The precise deposition of the coating materials has been achieved using technologies such as atomic layer deposition (ALD).[46] In this study, a conventional $Pd/Al_2O_3$ catalyst was coated with 45 layers of $Al_2O_3$ by alternately exposing the sample to trimethylaluminum (TMA) and water at 200 $^oC$. After calcination at 700 $^oC$ for 2 h, pores of about 2 nm in size were formed in the 8-nm thick $Al_2O_3$ coating as a result of dehydration under heating (Fig. 12D). The pores made the embedded Pd nanoparticles accessible to chemical species, as confirmed by CO chemisorption. When tested for the catalytic oxidative dehydrogenation of ethane (ODHE) to ethylene at 650 $^oC$,

the ethylene yield was increased by more than 10 folds (Fig. 12E). STEM images showed no visible morphology changes after reaction at 675 $^{o}$C for 28 h (Fig. 12F). In addition, the coke formed on the porous $Al_2O_3$-coated Pd/$Al_2O_3$ was reduced by 94% when compared to that on the uncoated sample. The sintering and coking resistance could be attributed to the blocking of low-coordination surface sites on the Pd nanoparticles.

**5.2 One-dimensional systems based on nanofibers and nanotubes**

Ceramic nanofibers and nanotubes are excellent supporting materials for metal-based catalytic nanoparticles because of their high specific surface areas, high thermal and chemical stability, and high mechanical strength. In an early study, it was demonstrated that a sinter-resistant catalytic system could be fabricated by depositing Pt nanoparticles on $TiO_2$ nanofibers, followed by coating with a porous sheath made of $SiO_2$ (Fig. 13A).[47] The porous $SiO_2$ shell could serve as an effective physical barrier to prevent the Pt nanoparticles from sintering, and at the same time, provided channels for chemical species to reach the active sites on the surface of Pt nanoparticles, allowing the catalytic reaction to occur. After $SiO_2$ coating, the average Pt dispersion only dropped from 42% to 29%, indicating that the Pt surface was largely unblocked. Indeed, the $SiO_2$-coated Pt nanoparticles did not show noticeable morphological changes upon calcination in air up to 750 $^{o}$C (Fig. 13B). At this temperature, the porous $SiO_2$ shell was still permeable to chemical species involved in the aqueous hydrogenation of Methyl red, with a catalytic conversion as high as 61% of the original catalyst (Fig. 13C).

Although the catalytic activity can be retained by generating pores in the protective layer to ensure accessibility, it is likely that the tiny pores can be easily blocked by impurities (*e.g.*, carbon) or collapse at elevated temperatures and pressures in real applications. In order to overcome these potential problems, a different approach was used for the fabrication of a sinter-resistant catalytic system without covering the metal surface while building an energy barrier around the catalytic nanoparticles. By simply reducing the coverage density of poly(vinylpyrrolidone) (PVP) on the Pt nanoparticles, $SiO_2$ could be selectively deposited on the $TiO_2$ support while leaving the Pt surface largely uncovered (Fig. 13D).[48] As such, the Pt surface was well exposed while the nanoparticles were supported on $TiO_2$ and isolated from each other by $SiO_2$. The competitive interactions of Pt with the strongly interacting $TiO_2$ support and the weakly interacting $SiO_2$ layer served an effective energy barrier, in addition to a physical barrier,

to inhibit the diffusion, migration, and coalescence of the Pt nanoparticles. As a result, the new triphasic catalytic system with an "islands in the sea" configuration showed significantly enhanced resistance to sintering up to 700 $^{o}$C while the Pt surface was kept fully exposed (Fig. 13E). Most importantly, the Pt catalyst was highly active in catalyzing the reduction of *p*-nitrophenol even after calcination at high temperatures (Fig. 13F).

A highly reactive and sinter-resistant catalytic system based on Pt nanoparticles embedded in the inner surfaces of $CeO_2$ hollow fibers ($Pt_{encap}/CeO_2$) was also demonstrated (Fig. 13G).[49] In this system, the polycrystalline $CeO_2$ sheath tightly surrounded the Pt nanoparticles with a maximal Pt-$CeO_2$ interaction for enhanced chemical bonding at the Pt-$CeO_2$ interfacial site, effectively stabilizing the Pt nanoparticles against sintering up to 700 $^{o}$C (Fig. 13H). The turnover frequency (TOF) of this catalytic system for low-temperature CO oxidation was found to be 2–3 orders of magnitude higher than those based on the conventional Pt/$SiO_2$ and Pt/$TiO_2$ systems (Fig. 13I).

**5.3 Two-dimensional systems based on nanosheets and ultrathin films**

Two-dimensional materials are attractive as supports for catalytic nanoparticles owing to their extraordinarily large specific surface areas. For instance, graphene sheets have a theoretical specific surface area of 2,630 $m^2/g$. Sinter-resistant catalysts involving graphene-supported, ultrafine metal nanoparticles have recently been demonstrated.[50] As shown in Fig. 14A, the Pt nanoparticles were sandwiched between reduced graphene oxide (rGO) and mesoporous $SiO_2$ ($mSiO_2$) layers. The 1.65-nm Pt nanoparticles remained almost unchanged after heat treatment at 700 $^{o}$C in Ar for 2 h (Fig. 14B). The robust mesoporous $SiO_2$ layer not only physically confined the ultrafine metal nanoparticles but also prevented the graphene supports from aggregation to maintain the large surface area. When used for CO oxidation, this catalyst showed a conversion ratio of 6.8% and complete conversion could be reached at 120 $^{o}$C (Fig. 14C). The CO conversion for the water gas shift (WGS) reaction over the Pt-rGO@$mSiO_2$ catalyst at 450 $^{o}$C remained almost unchanged at *ca.* 30% over a period of about 80 h, demonstrating its excellent stability against sintering. In particular, the excellent thermal stability allows for the achievement of 100 % catalytic conversion even after a detoxification process for the thermal combustion of poisonous molecules, which is impossible for bare Pt nanoparticles due to their quick sintering during the treatment.

Supporting metal nanoparticles on 2D metal oxides with a proper surface structure allows one to control what kind of atomic structure will be presented on the surface. As a result, it is feasible to elucidate the sintering mechanism and further figure out an effective strategy to ensure that the support will expose the right surface at the highest possible fraction. A number of model catalysts have been developed by depositing metal nanoparticles on structurally well-defined oxides from the vapor phase. In one study, four oxides were used as the supports for Ag nanoparticles, including two 4-nm $CeO_2(111)$ films with different extents of surface reduction (x = 0.1 and 0.2 in $CeO_{2-x}$); one 1-nm $CeO_{1.9}(111)$ film; and one 4-nm MgO(100) film.[16] The $E_{adh}$ for Ag nanoparticles with $CeO_2(111)$ was much greater than that with MgO(100), and this value increased with the extent of reduction for the $CeO_2$ (Fig. 14D). The Ag adatoms bind more than 100 kJ/mol more strongly to the vacancy sites on $CeO_{2-x}(111)$ than to the stoichiometric sites. The effect of different support materials on the energy diagram for the sintering of Ag nanoparticles is summarized in Fig. 14E. The thermodynamic driving force for sintering of 400-atom Ag particles (3 nm in diameter) was much lower on the slightly reduced $CeO_2(111)$ surface than on MgO(100) due to the extra stability offered by the strength of chemical bonding ($E_{adh}$) between the Ag nanoparticles and the underlying oxide surface.

The sinter-resistant catalytic systems based on ultrathin films also provide a simple platform for *in situ* monitoring of thermal durability against sintering under realistic reaction conditions. In a recent example, it was shown that PtRh alloy nanoparticles supported on a model $Al_2O_3(001)$ ultrathin film had excellent sinter-resistance when applied to CO oxidation at atmospheric pressure (Fig. 14F).[10] The composition-dependent restructuring of alloy nanoparticles on $Al_2O_3(001)$ surface was also elucidated by employing high-energy grazing incidence X-ray diffraction as an *in situ* probe. The Pt-rich alloy nanoparticles essentially grew vertically along the direction perpendicular to the surface as a result of the strong tendency for the particles to evolve into a 3D equilibrium shape (Fig. 14G). The addition of Rh gave rises to an advantageous, higher dispersion and the increased mismatch to the $Al_2O_3(001)$ planer surface promoted a more 3D shape, closer to the equilibrium shape.

## 6. Concluding remarks and perspectives

Despite the remarkable progress, stabilization of supported metal nanoparticles against sintering still faces a number of major challenges that need to be addressed. Most of prior studies

have focused on the thermal stability of supported metal nanoparticles at relatively low temperatures (<600 $^{o}$C) for reactions such as CO oxidation. There is rarely a reported demonstration of supported metal nanoparticles with satisfactory thermal stability at temperatures above 800 $^{o}$C. However, heterogeneous catalysts with good thermal stability at temperatures >800 $^{o}$C are in great demand for various environment protection and chemical conversion processes (*e.g.*, automobile exhaust control, petroleum refinery, and combustion of methane).

Both the sintering kinetics and catalytic activity are correlated with the chemical potentials of atoms on metal nanoparticles. It is true that decreasing the chemical potential could effectively slow down the sintering rate, but it may undesirably decrease the catalytic activity. For instance, the most mobile atoms on nanoparticles are situated at corners and edges, with low coordination numbers, but they are also the most active sites for the initiation of sintering. Selectively capping these sites can inhibit the sintering to a certain extent, but unavoidably deactivate the most viable sites in terms of catalytic activity and selectivity. How to balance the sinter-resistance with both catalytic activity and selectivity is crucial to the achievement of rationally designed catalysts with long lifetime.

Although significant progress has been made in *in situ* characterization, the sintering process remains incompletely understood. Highly sensitive *in situ* tools with superb temporary and spatial resolutions are needed for direct observation of single atom/molecule diffusion on support surface, as well as alternation to the pore structure in the protective layer. In general, both direct and indirect characterization tools are required to resolve the sintering mechanism/pathway. Furthermore, integration of experimental and computational efforts is needed to validate and establish the dynamic model involved in a sintering process. The integration will offer deep insights into the mass transfer and sintering dynamics of individual metal nanoparticles. Recent achievements in theoretically predicting stable metal and/or support structures should eventually aid in the rational design of sinter-resistant catalysts with the right composition, shape, and metal-support interaction. The current understanding of sintering has been largely gained from carefully controlled model systems based on flat substrates, which are kind of different from those used in practical catalysts. Future studies should be directed toward conditions resembling the real catalytic applications.

Bottom-up approaches at the single-nanoparticle level typically suffer from challenges

related to large-scale production and commercial application. The synthesis of such nanomaterials usually involves a multi-step process, thus the development of simplified synthesis strategies with high yields and good reproducibility is required. In addition, the ALD method often requires expensive equipment and can hardly be used to produce the fine structures at a cost-effective manner. Recently, continuous flow synthesis has emerged as an attractive platform for the scalable, large-volume production of catalytic systems based on nanoparticles.

The last but not least, recent development of metal nanoparticles with well-defined and controllable sizes, shapes, compositions, structures, and other properties offers a new opportunity to investigate their properties as functions of these parameters, showing great potential for a variety of applications related to catalysis. In terms of sintering, early effort has focused on the depression of particle size growth, while less attention was paid to the mitigation of shape reconstruction under harsh conditions although shape plays a critical role in determining catalytic activity and selectivity. More attention should be paid to the establishment of correlation between the shape reconstruction and the variation in activity/selectivity during the sintering process. Taken together, the advances in understanding the sintering of supported metal nanoparticles will have a profound impact on the development of cost-effective catalytic systems with an optimal catalytic activity and long-term stability for environment protection and energy conversion.

## Conflicts of interest

There is no conflicts of interest to declare.

**Acknowledgement**

Y.D. was partially supported by the National Natural Science Foundation of China (21201034), Natural Science Foundation of Jiangsu Province (BK20171153), and the Fundamental Research Funds for the Central Universities. Y.X. was partially supported by Toyota Motor Engineering and Manufacturing North America, the National Science Foundation (CMMI-1634687), and startup funds from the Georgia Institute of Technology. C.T.C. gratefully acknowledges financial support for this work by DOE-OBES Chemical Sciences Division under grant #DE-FG02-96ER14630.

## Notes and references


1 S. Xie, S. Choi, X. Xia and Y. Xia, *Curr. Opin. Chem. Eng.*, 2013, **2**, 142–150.

2 C. T. Campbell, *Acc. Chem. Res.*, 2013, **46**, 1712–1719.

3 C. T. Campbell and J. R. V. Sellers, *Faraday Discuss.*, 2013, **162**, 9–30.

4 E. D. Goodman, J. A. Schwalbe and M. Cargnello, *ACS Catal.*, 2017, **7**, 7156–7173.

5 C. H. Bartholomew, *Appl. Catal. A-Gen.*, 2001, **212**, 17–60.

6 C. T. Campbell, *Nat. Chem.*, 2012, **4**, 597-598.

7 K. Morgan, A. Goguet and C. Hardacre, *ACS Catal.*, 2015, **5**, 3430–3445.

8 L. Luo, M. H. Engelhard, Y. Shao and C. Wang, *ACS Catal.*, 2017, **7**, 7658–7664.

9 K. Wettergren, F. F. Schweinberger, D. Deiana, C. J. Ridge, A. S. Crampton, M. D. Rötzer, T. W. Hansen, V. P. Zhdanov, U. Heiz and C. Langhammer, *Nano Lett.*, 2014, **14**, 5803–5809.

10 U. Hejral, P. Müller, O. Balmes, D. Pontoni and A. Stierle, *Nat. Comm.*, 2016, **7**, 10964.

11 L. D. Marks and L. Peng, *J. Phys.: Condens. Matter*, 2016, **28**, 053001.

12 S. L. Hemmingson and C. T. Campbell, *ACS Nano*, 2017, **11**, 1196–1203.

13 C. T. Campbell and Z. Mao, *ACS Cat.*, 2017, **7**, 8460–8466.

14 C. T. Campbell, S. C. Parker and D. E. Starr, *Science*, 2002, **298**, 811–814.

15 S. C Parker and C. T. Campbell, *Phys. Rev. B*, 2007, **75**, 035430.

16 J. A. Farmer and C. T. Campbell, *Science*, 2010, **329**, 933–936.

17 M. Bowker, *Nat. Mater.*, 2002, **1**, 205-206.

18 T. W. Hansen, A. T. Delariva, S. R. Challa and A. Datye, *Acc. Chem. Res.*, 2013, **46**, 1720–1730.

19 K. J. Hu, S. R. Plant, P. R. Ellis, C. M. Brown, P. T. Bishop and R. E. Palmer, *J. Am. Chem. Soc.*, 2015, **137**, 15161–15168.

20 G. Tammann, *Z. Anorg. Allg. Chem.*, 1919, **107**, 1–239.

21 G. Prieto, H. Tüysüz, N. Duyckaerts, J. Knossalla, G. Wang and F. Schüth, *Chem. Rev.*, 2016, **116**, 14056–14119.

22 P. Buffat and J. P. Borel, *Phys. Rev. A*, 1976, **13**, 2287-2298.

23 S. Porsgaard, L. R. Merte, L. K. Ono, F. Behafarid, J. Matos, S. Helveg, M. Salmeron, B. Roldan Cuenya and F. Besenbacher, *ACS Nano*, 2012, **6**, 10743–10749.

24 L. R. Houk, S. R. Challa, B. Grayson, P. Fanson and A. K. Datye, *Langmuir*, 2009, **25**,

11225−11227.

25 D. S. Su, B. Zhang and R. Schlögl, *Chem. Rev.*, 2015, **115**, 2818–2882.

26 P. T. Z. Adibi, F. Mazzotta, T. J. Antosiewicz, M. Skoglundh, H. Grönbeck and C. Langhammer, *ACS Catal.*, 2015, **5**, 426–432.

27 K. D. Gilroy, A. Elnabawy, T. H. Yang, L. Roling, J. Howe, M. Mavrikakis and Y. Xia, *Nano Lett.*, 2017, **17**, 3655–3661.

28 G. S. Parkinson, Z. Novotny, G. Argentero, M. Schmid1, Jiří Pavelec, R. Kosak, P. Blaha and U. Diebold, *Nat. Mater.*, 2013, **12**, 724–728.

29 S. B. Simonsen, I. Chorkendorff, S. Dahl, M. Skoglundh, J. Sehested and S. Helveg, *J. Am. Chem. Soc.*, 2010, **132**, 7968–7975.

30 S. R. Challa, A. T. Delariva, T. W. Hansen, S. Helveg, J. Sehested, P. L. Hansen, F. Garzon and A. K. Datye, *J. Am. Chem. Soc.*, 2011, **133**, 20672–20675.

31 S. Zhang, C. Chen, M. Cargnello, P. Fornasiero, R. J. Gorte, G. W. Graham and X. Pan, *Nat. Comm.*, 2015, **6**, 7778.

32 N. Lu, J. Wang, S. Xie, Y. Xia and M. J. Kim, *Chem. Comm.*, 2013, **49**, 11806–11808.

33 C. W. Han, P. Majumdar, E. E. Marinero, A. Aguilar-Tapia, R. Zanella, J. Greeley and V. Ortalan, *Nano Lett.*, 2015, **15**, 8141–8147.

34 B. Qiao, A. Wang, X. Yang, L. F. Allard, Z. Jiang, Y. Cui, J. Liu, J. Li and T. Zhang, *Nat. Chem.*, 2011, **3**, 634–641.

35 J. Jones, H. Xiong, A. T. DeLaRiva, E. J. Peterson, H. Pham, S. R. Challa, G. Qi, S. Oh, M. H. Wiebenga, X. I. P. Hernández, Y. Wang and A. K. Datye, *Science*, 2016, **353**, 150–154.

36 C. Carrillo, A. DeLaRiva, H. Xiong, E. J. Peterson, M. N. Spilde, D. Kunwar, R. S. Goeke, M. Wiebenga, S. H. Oh, G. Qi, S. R. Challa, A. K. Datye, *Appl. Catal. B: Environ.*, 2017, **218**, 581-590.

37 W. Li, L. Kovarik, D. Mei, J. Liu, Y. Wang and C. H. F. Peden, *Nat. Comm.*, 2013, **4**, 2481.

38 Q. Zhang, I. Lee, J. B. Joo, F. Zaera and Y. Yin, *Acc. Chem. Res.*, 2013, **46**, 1816–1824.

39 K. An, Q. Zhang, S. Alayoglu, N. Musselwhite, J. Shin and G. A. Somorjai, *Nano Lett.*, 2014, **14**, 4907–4912.

40 M. Cargnello, J. J. D. Jaén, J. C. H. Garrido, K. Bakhmutsky, T. Montini, J. J. C. Gámez, R. J. Gorte and P. Fornasiero, *Science*, 2012, **337**, 713–717.

41 H. Tang, F. Liu, J. Wei, B. Qiao, K. Zhao, Y. Su, C. Jin, L. Li, J. Liu, J. Wang and T. Zhang,

*Angew. Chem. Int. Ed.*, 2016, **55**, 10606–10611.

42 W. Zhan, Y. Shu, Y. Sheng, H. Zhu, Y. Guo, L. Wang, Y. Guo, J. Zhang, G. Lu and S. Dai, *Angew. Chem. Int. Ed.*, 2017, **129**, 4565–4569.

43 B. K. Min, W. T. Wallace and D. W. Goodman, *J. Phys. Chem. B*, 2004, **108**, 14609–14615.

44 Y. Yin, Y. Lu, B. Gates and Y. Xia, *Chem. Mater.*, 2001, **13**, 1146–1148.

45 H. Zhao, D. Wang, C. Gao, H. Liu, L. Hand and Y. Yin, *J. Mater. Chem. A*, 2016, **4**, 1366–1372.

46 J. Lu, B. Fu, M. C. Kung, G. Xiao, J. W. Elam, H. H. Kung and P. C. Stair, *Science*, 2012, **335**, 1205–1208.

47 Y. Dai, B. Lim, Y. Yang, C. M. Cobley, W. Li, E. C. Cho, B. Grayson, P. T. Fanson, C. T. Campbell, Y. Sun and Y. Xia, *Angew. Chem., Int. Ed.*, 2010, **49**, 8165–8168.

48 P. Lu, C. T. Campbell and Y. Xia, *Nano Lett.*, 2013, **13**, 4957–4962.

49 K. Yoon, Y. Yang, P. Lu, D. Wan, H. Peng, K. S. Masias, P. T. Fanson, C. T. Campbell and Y. Xia, *Angew. Chem. Int. Ed.*, 2012, **51**, 9543–9546.

50 L. Shang, T. Bian, B. Zhang, D. Zhang, L. Wu, C. Tung, Y. Yin and T. Zhang, *Angew. Chem. Int. Ed.*, 2014, **53**, 250–254.

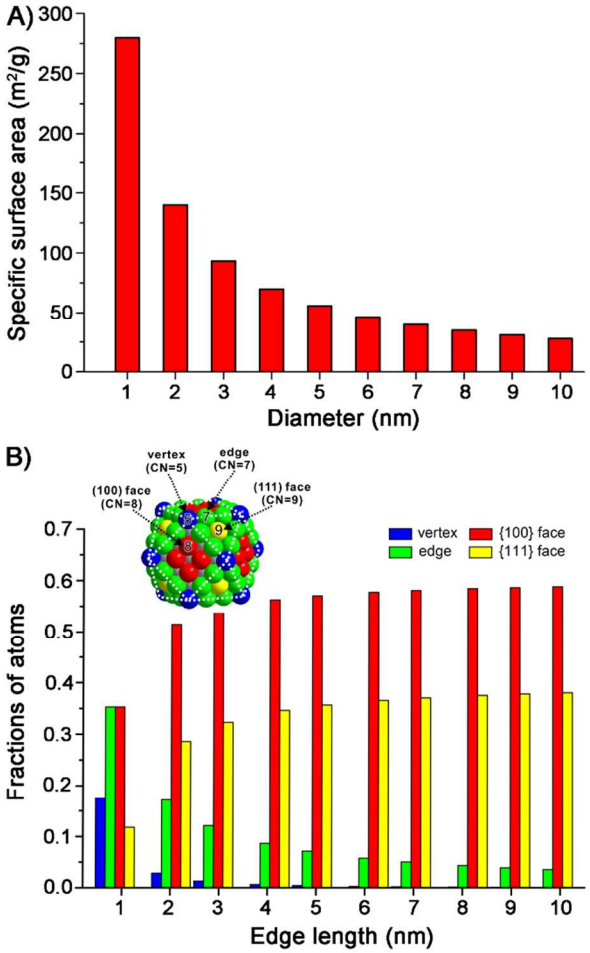


**Figure 1.** The importance of particle size in determining the performance of a catalyst. (A) Plot of the specific surface area as a function of the diameter of Pt spherical nanoparticles. (B) Fractions of different types of surface atoms (vertex, edge, and face) as a function of the edge length for Au cuboctahedra (see the inset for an atomic model, together with the different types of surface atoms and their coordination numbers). Modified with permission from ref. 1, copyright 2013 Elsevier.

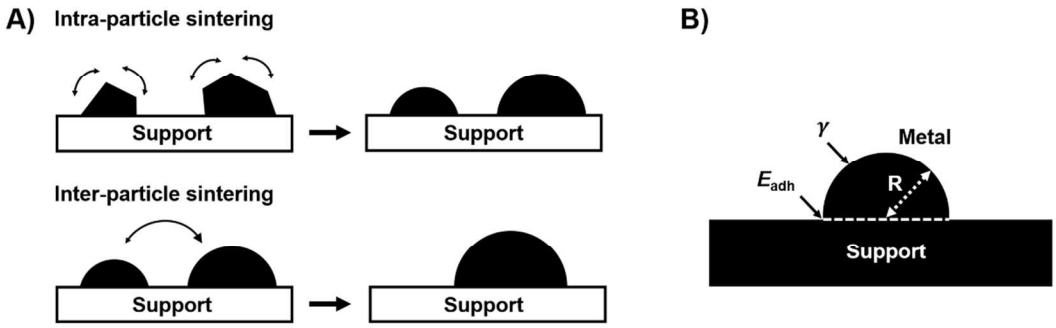


**Figure 2.** Schematic illustrations of sintering and the driving forces involved. (A) Comparison of intra- and inter-particle sintering, with the use of hemispheres to represent the equilibrium shape of supported nanoparticles, which can be actually determined using the Winterbottom construction. (B) Illustrations of parameters that determine the chemical potential of atoms on the surface of a metal nanoparticle supported on a substrate.

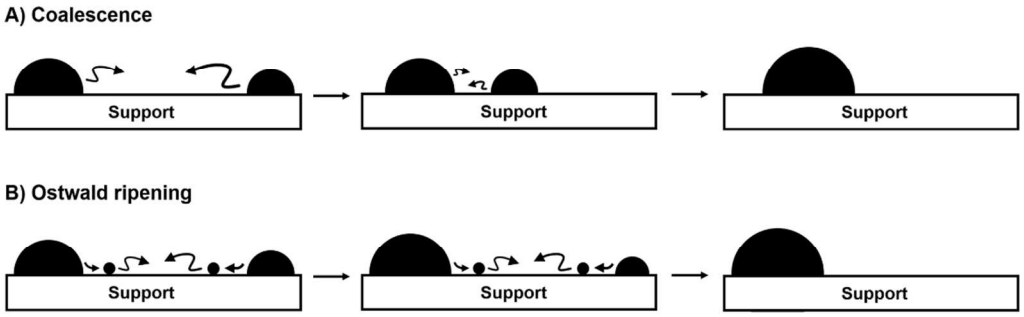


**Figure 3.** Schematic illustrations of the two principal sintering mechanisms or pathways for inter-particle sintering: (A) coalescence (Smoluchowski ripening) and (B) Ostwald ripening, respectively.

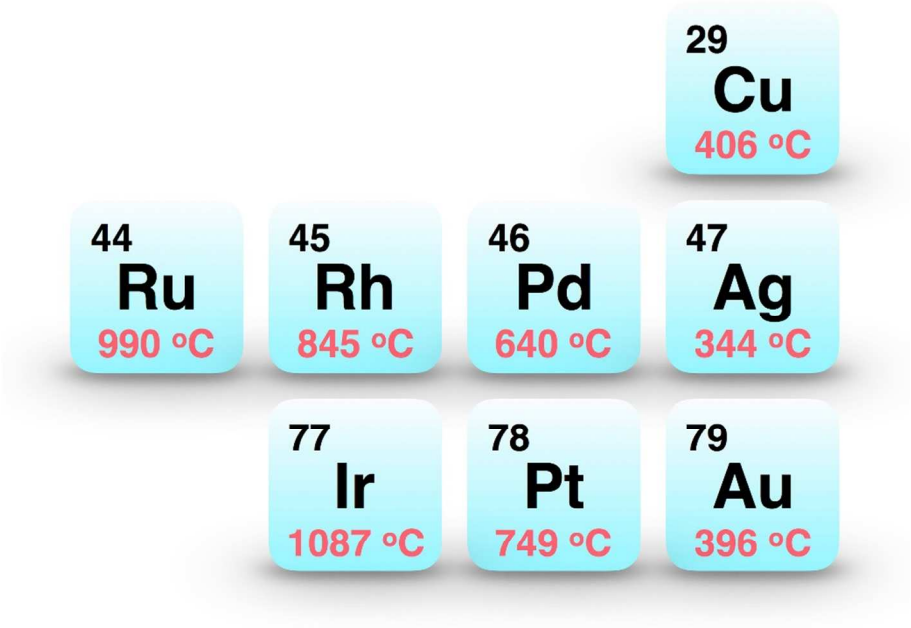


**Figure 4.** Comparison of the Tamman temperatures ($^{o}$C) for the precious metals commonly used in heterogeneous catalysis.

**Table 1** Summary of the advanced techniques for studying sintering process (information taken from ref. 2-4, 9, 13, 14, 25, 26)

| Techniques | Pros | Cons |
|---|---|---|
| *In situ* TEM | *i*) Practical/model catalyst<br>*ii*) Dynamic changes (*e.g.*, size, shape, structure, and lattice spacing)<br>*iii*) Single-particle level with atomic resolution<br>*iv*) Convenient combination with spectroscopy (*e.g.*, EDX and EELS)<br>*v*) Environmental gaseous/liquid conditions (*e.g.*, CO, $O_2$, $H_2O$ vapor, air, and liquid) | *i*) Electron-beam damage<br>*ii*) Limited upper pressure of ~10 mbar |
| *In situ* STM | *i*) Dynamic surface changes (*e.g.*, electronic structure, coordination environment, and chemical bonds)<br>*ii*) Environmental gaseous conditions (*e.g.*, CO, and $O_2$)<br>*iii*) Single-particle level at atomic resolution | *i*) Model catalyst only<br>*ii*) Difficult to track sintered aggregates<br>*iii*) Limited upper pressure of ~0.1 mbar |
| *In situ* XPS | *i*) Practical/model catalyst<br>*ii*) Dynamic surface changes (*e.g.*, oxidation state, and composition)<br>*iii*) Statistical information of ensemble<br>*iv*) Environmental gaseous conditions (*e.g.*, $O_2$, and $H_2$) | *i*) Limited depth of the top few atomic layers<br>*ii*) Limited upper pressure of ~1 mbar |
| *In situ* INPS | *i*) Facile operation at ambient pressure<br>*ii*) Dynamic changes in sizes in sub-second range<br>*iii*) Statistical information of ensemble | *i*) Model catalyst<br>*ii*) Additional correlation with ex situ TEM analysis<br>*iii*) Complex fabrication |

| | | |
|---|---|---|
| | *iv*) Environmental gaseous conditions (*e.g.*, $O_2$, $H_2$, and $NO_2$) | procedure of sensor chips |
| Metal atom adsorption microcalorimetry | *i*) High accuracy in metal-support bonding energy measurements<br>*ii*) Provides metal/support adhesion energy and metal atom chemical potential vs particle size for ensemble average | *i*) Limited to planar support<br>*ii*) Only probes ensemble average, not single particle<br>iii) Limited to UHV, no *in situ* observation nor environmental conditions |

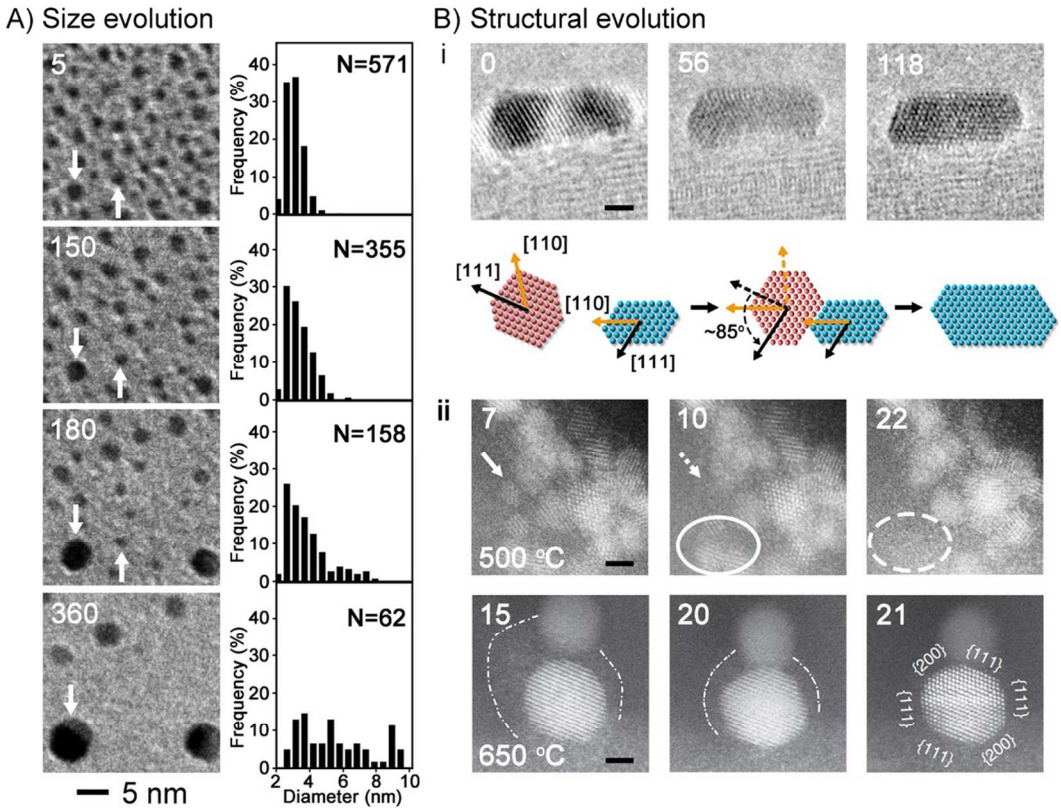


**Figure 5.** Monitoring sintering process by *in situ* environment transmission electron microscopy (ETEM). (A) Time-lapsed TEM images recorded *in situ* and the corresponding size distribution of a $Pt/Al_2O_3$ model catalyst during exposure to 10 mbar of air at 650 $^oC$. The number in each panel indicates the elapsed time in minute. Ref. 29, copyright 2010 American Chemical Society. (B) (i) time-lapsed TEM images of two Pt nanoparticles supported on a carbon nanotube at 100 $^oC$ under $O_2$, and a schematic illustration of reoriented attachment. The number in each panel indicates the elapsed time in second (scale bar: 1 nm). Modified with permission from ref. 8, copyright 2017 American Chemical Society. (ii) Sequential images showing the dissociation of 2-3 nm particles and the formation of atom "clouds" during calcination at 500 and 650 $^oC$, respectively, under $O_2$. The number in each panel indicates the elapsed time in minute (scale bars: 2 nm). Modified with permission from ref. 31, copyright 2015 Springer Nature.)

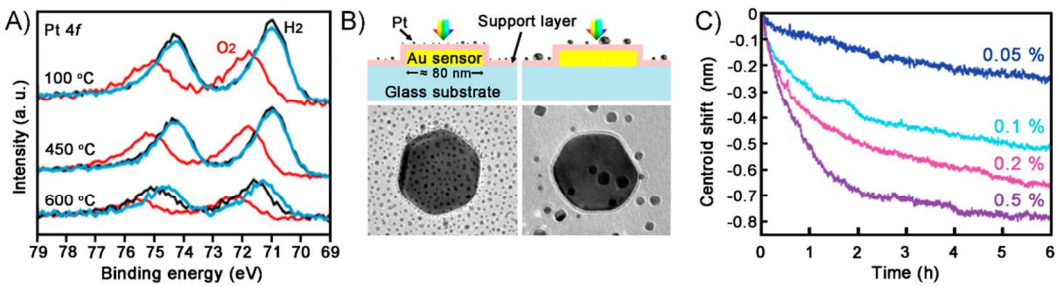


**Figure 6.** Monitoring of sintering by *in situ* spectroscopy methods. (A) Series of Pt 4*f* XPS spectra recorded under 0.5 Torr of $H_2$ at 400 °C (black), 0.5 Torr of $H_2$ at the indicated temperature (blue), and 0.5 Torr of $O_2$ at the indicated temperature (red). Modified with permission from ref. 23, copyright 2012 American Chemical Society. (B) Schematic illustration and the corresponding TEM images of an indirect nanoplasmonic sensing (INPS) platform (left) before and (right) after sintering treatment under $O_2$ at 600 °C for 12 h. (C) The refractive index-normalized INPS centroid shift signal during the sintering of Pt nanoparticles supported on $SiO_2$ as a model catalyst under atmospheric pressure involving four different $O_2$ concentrations in Ar. Modified with permission from ref. 26, copyright 2015 American Chemical Society.

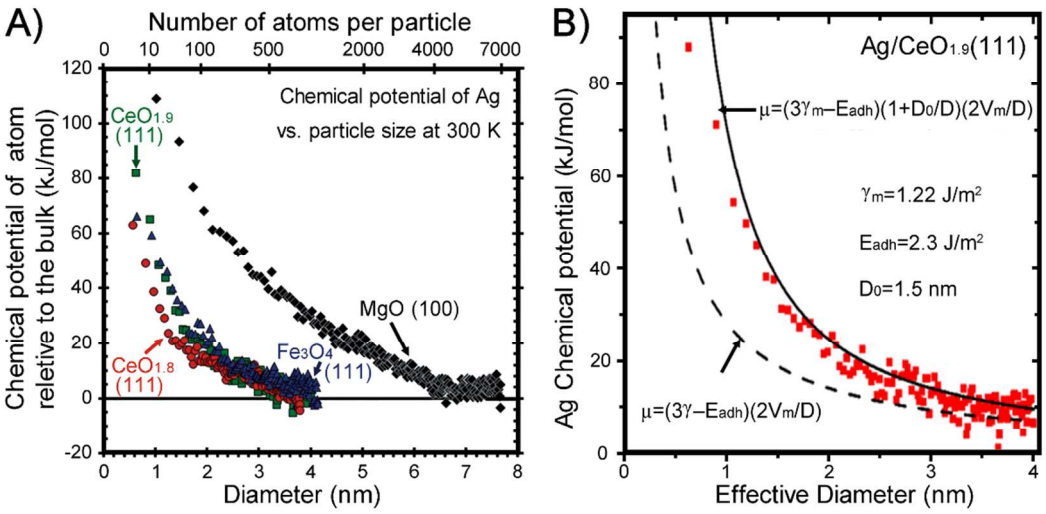


**Figure 7.** (A) The chemical potential of Ag atoms on Ag nanoparticles, which were supported on different oxide surfaces, as a function of the average particle size. Adopted with permission from ref. 3, copyright 2013 Royal Chemistry Society. (B) The chemical potential of Ag atoms on Ag nanoparticles supported on a slightly reduced $CeO_2$(111) surface as a function of particle size, and the fitting curves based on Eq. (1) and Eq. (2), respectively. Adopted with permission from ref. 13, copyright 2017 American Chemical Society.

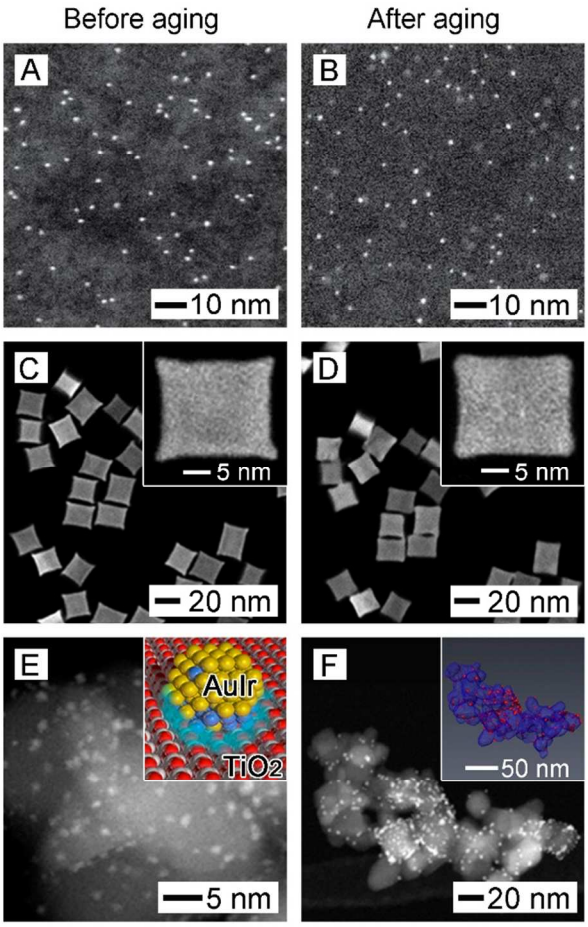


**Figure 8.** Control of the uniformity in size, shape, and composition of metal nanoparticles to improve their thermal stability. (A, B) STEM images of the size-selected $Pt_{68}$ clusters supported on $SiO_2$ (A) before and (B) after the hydrogen oxidation reaction. Modified with permission from ref. 9, copyright 2014 American Chemical Society. (C, D) Representative HAADF-STEM images of Rh-Pd core-frame nanocubes (C) before and (D) after heating to 500 $^{o}$C for 1 h, with the insets showing a schematic illustration of the core-frame structure and an individual Pd-Rh nanocube, respectively. Modified with permission from ref. 32, 2013 Royal Society of Chemistry. (E, F) The HAADF-STEM images of AuIr bimetallic nanoparticles on $TiO_2$ support (E) before and (F) after activation at 500 $^{o}$C under $H_2$ for 2 h, with the inset showing the corresponding atomic model and an STEM tomogram, respectively. Modified with permission from ref. 33, copyright 2015 American Chemical Society.

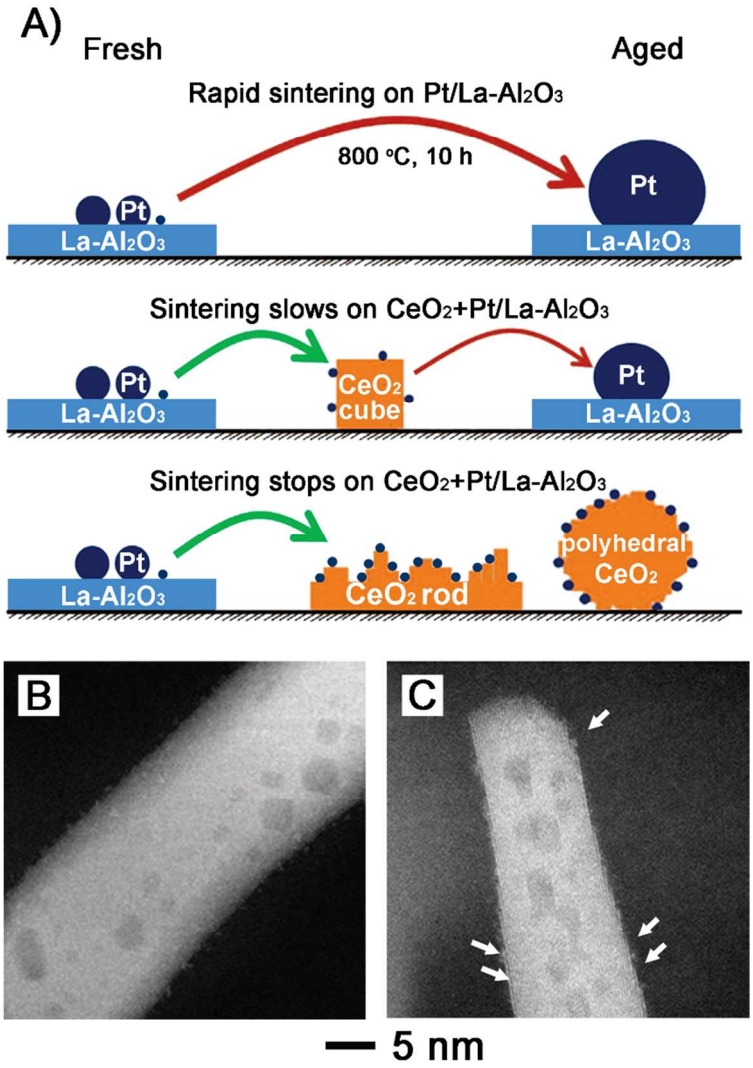


**Figure 9.** (A) Illustration of the sintering of Pt nanoparticles, showing how ceria can trap the emitted Pt as volatile $PtO_2$ to suppress sintering. (B) Representative AC-STEM images of 1 wt % $Pt/CeO_2$-rod after aging (heat treatment) at 800 °C for 10 h under air flow. (C) HAADF AC-STEM image of the sample in (B) after three cycles of CO oxidation to 300 °C. The arrows point to step edges that appear to be the sites where the Pt species are present. Modified with permission from ref. 35, copyright 2016 American Association for the Advancement of Science.

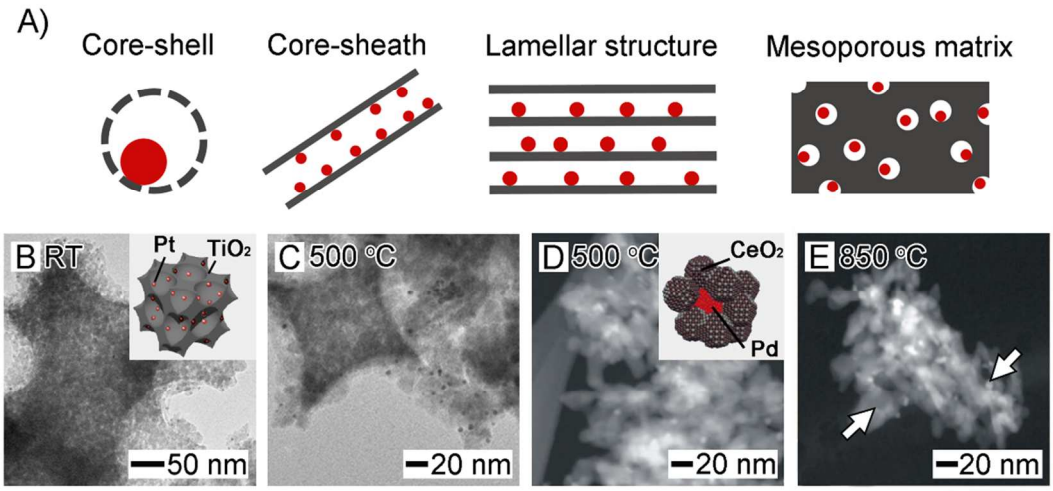


**Figure 10.** (A) Schematic illustration of metal nanoparticles under physical confinement. TEM images of Pt nanoparticles confined in $TiO_2$ mesoporous matrix (B) before and (C) after *n*-hexane reforming reaction at 500 °C, with the inset showing a schematic of the Pt/$TiO_2$ structure. Modified with permission from ref. 39, copyright 2014 American Chemical Society. (D, E) Thermally stable Pd/$CeO_2$ core-shell structures as single units on the surface of a modified $Al_2O_3$ support. HAADF-STEM images of the structures after calcination at (D) 500 $^oC$ (inset: atomic model of a Pd/$CeO_2$ core-shell unit) and (E) 850 $^oC$, respectively, for 5 h. Modified with permission from ref. 40, copyright 2012 American Association for the Advancement of Science.

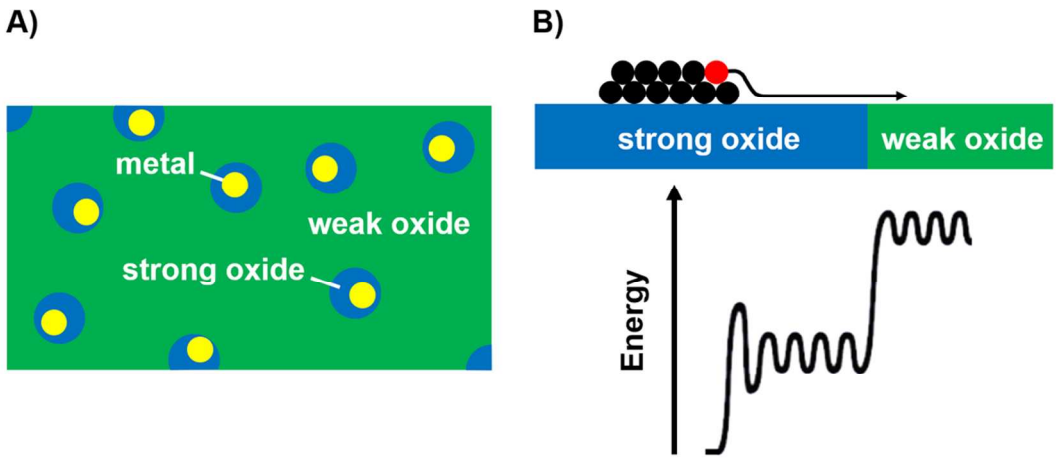


**Figure 11.** (A) Schematic representation of metal nanoparticles supported on the surface of a two-phase oxide support containing separate domains of two oxides that bind to the metal weakly and strongly, respectively. (B) Diagram showing the atomic structure at the edge of one of the metal nanoparticles, and the energy barriers associated with moving the red metal atom off the edge of the nanoparticle and across the oxide surface along the path shown.

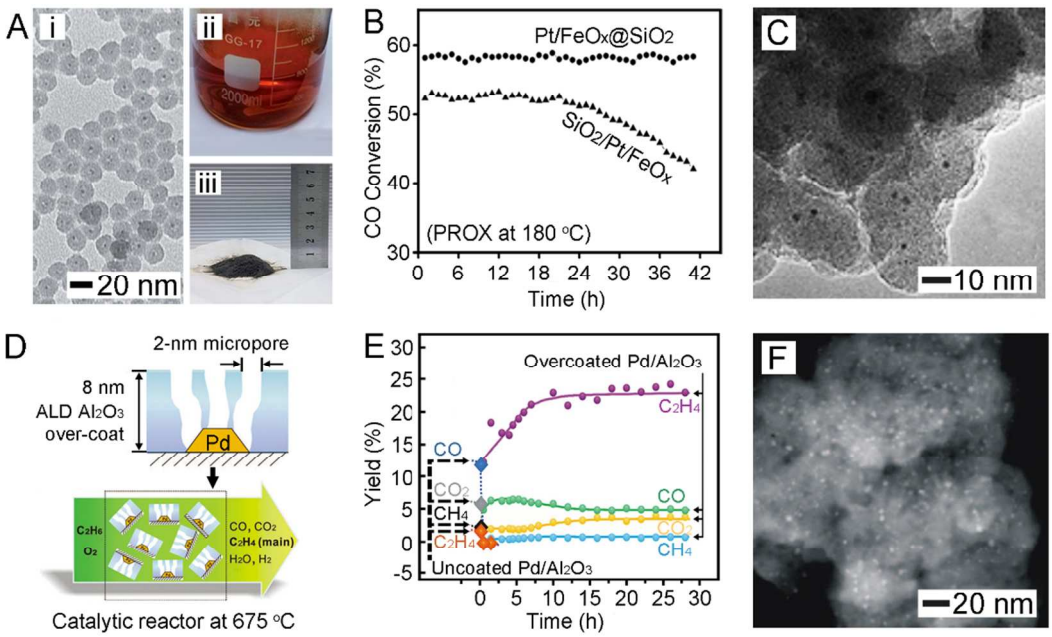


**Figure 12.** (A) Large-scale production of the $Pt/FeO_x@SiO_2$ core-shell structure: (i) TEM image, photographs of (ii) the reaction system with a total volume of 800 mL and (iii) the final product (powder). The ruler for reference is in centimeter. (B) Plots of CO conversion versus reaction time. (C) TEM image of the $Pt/FeO_x@SiO_2$ after PROX reaction at 100 $^oC$ for 84 h. Modified with permission from ref. 45, copyright 2016 Royal Society of Chemistry. (D) A schematic model of the $Pd/Al_2O_3$ catalyst, with a $Al_2O_3$ overcoat by ALD, during oxidative dehydrogenation of ethane (ODHE) at 675 $^oC$. (E) Product yields on the $Pd/Al_2O_3$ samples with and without the ALD $Al_2O_3$ overcoat during ODHE as a function of reaction time under identical conditions. Diamonds with a dashed line, product yields on the uncoated $Pd/Al_2O_3$ sample; circles with solid lines, product yields on the $45Al/Pd/Al_2O_3$ sample. (F) STEM image of the $45Al/Pd/Al_2O_3$ sample after use at 675 °C for about 1700 min. Modified with permission from ref. 46, copyright 2012 American Association for the Advancement of Science.

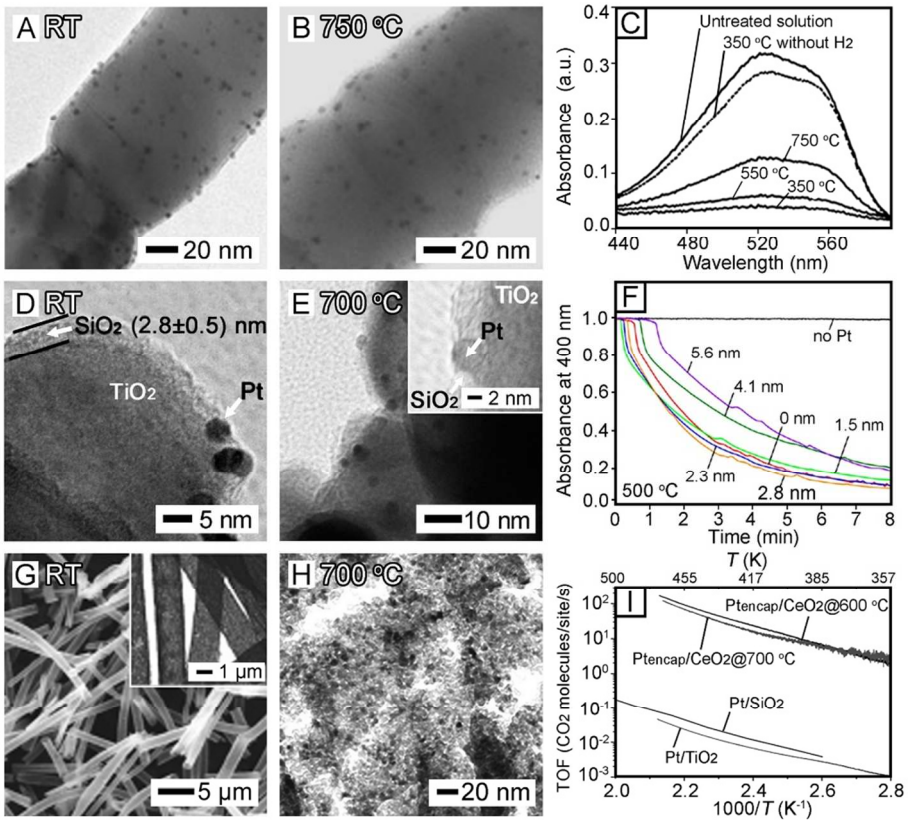


**Figure 13.** Three representative examples of sinter-resistant catalysts based on one-dimensional nanofibers and nanotubes. TEM images of Pt nanoparticles supported on a $TiO_2$ nanofiber and coated by a porous sheath of $SiO_2$ (A) before and (B) after calcination at 750 $^oC$ in air for 2 h, and (C) UV-Vis spectra of a methyl red solution before and after hydrogenation in the presence of the porous-$SiO_2$/Pt/$TiO_2$ nanofibers aged at different temperatures. Modified with permission from ref. 47, copyright 2010 Wiley-VCH. TEM images showing the selectivity of $SiO_2$ deposition onto the surface of $TiO_2$ *versus* the surface of Pt nanoparticles with an "island-in-the-sea" configuration (D) before (E) after calcined at 700 $^oC$ for 2 h, and (F) the normalized absorbance at 400 nm for the reaction solution (*p*-nitrophenol and $NaBH_4$) *versus* reaction time after the addition of Pt/$TiO_2$-$SiO_2$ catalysts (with the $SiO_2$ thicknesses being 1.5, 2.3, 2.8, 4.1, and 5.6 nm, respectively) and after calcination at 500 °C in air for 2 h. Modified with permission from ref. 48, copyright 2013 American Chemical Society. (G) SEM image of Pt nanoparticles embedded in $CeO_2$ (Pt/$CeO_2$) nanotubes with the inset showing a TEM image, (H) TEM image of the Pt/$CeO_2$ nanotubes after calcination in air at 700 $^oC$. (I) Turnover frequencies (TOFs) at an $O_2$/CO ratio of 1:2 *versus* temperature for the Pt/$CeO_2$ nanotubes calcined at 600 and 700 $^oC$, respectively, for 2 h. Modified with permission from ref. 49, copyright 2012 Wiley-VCH.

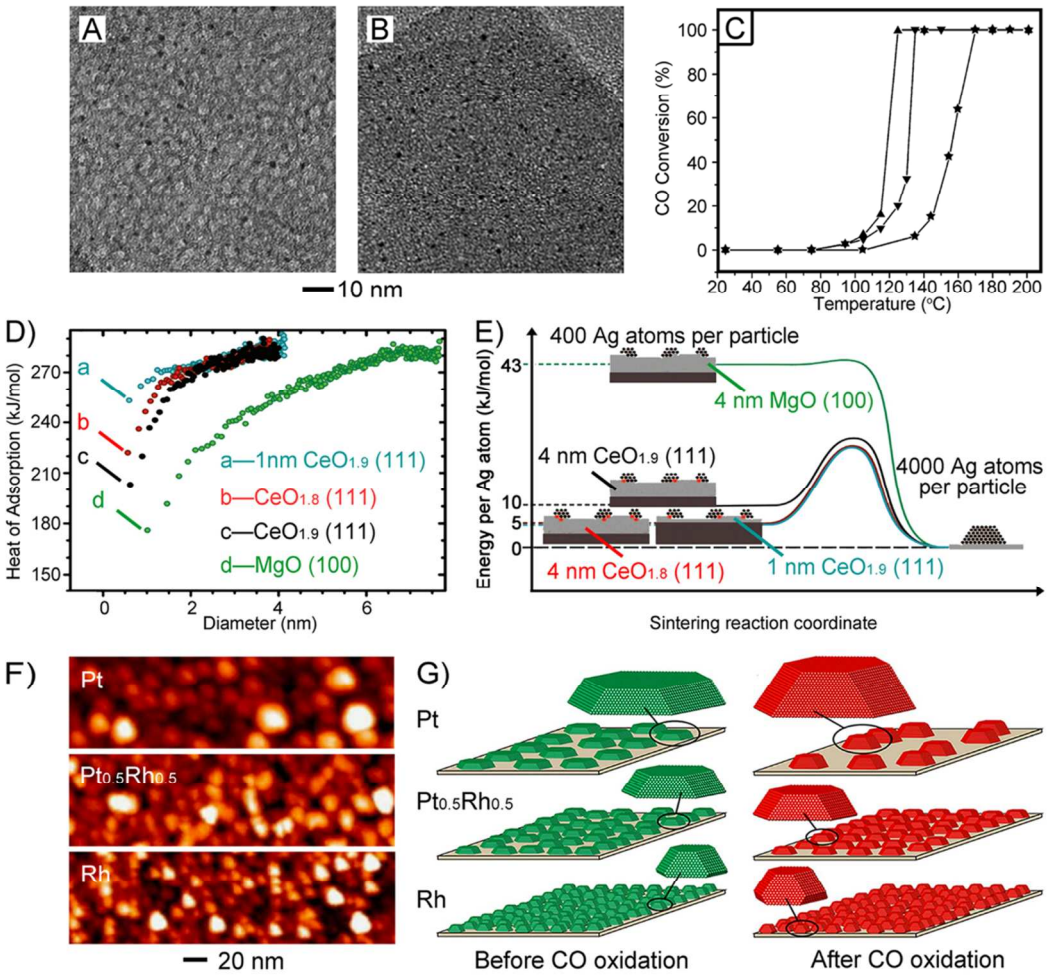


**Figure 14.** TEM images of graphene-supported ultrafine Pt nanoparticles, which were further encapsulated in mesoporous $SiO_2$ layer (Pt-rGO@m$SiO_2$), (A) before and (B) after aging (heat treatment) at 700 $^oC$ under Ar for 2 h. (C) Catalytic activities of the Pt-rGO@m$SiO_2$ post calcination at 500 $^oC$ (▲) and 700 $^oC$ (▼), respectively, towards CO oxidation. A sample without calcination (★) was also included for comparison. Modified with permission of ref. 50, copyright Wiley-VCH. (D) Measured heat of adsorption for Ag atoms as a function of the Ag particle diameter to which the atoms are added, for four different surfaces. (E) Schematics showing the differences in energetics for the sintering of Ag nanoparticles supported on different substrates. Modified with permission of ref. 16, copyright 2010 American Association for the Advancement of Science. (E) AFM images of Pt, $Pt_{0.5}Rh_{0.5}$, and Rh deposited on ultrathin films under UHV after the CO oxidation experiments. (F) Schematic illustration of representative particle shape and sample morphology before and after sintering as deduced from the Bragg peak. Modified with permission of ref. 10, copyright 2016 Springer Nature.

## Author biography

*Yunqian Dai received her Ph.D. in Materials Chemistry and Physics from Southeast University in 2011 with Prof. Yueming Sun. She spent two years in the Xia group as a visiting graduate student from 2008–2010. She is now an Associate Professor in the School of Chemistry and Chemical Engineering at Southeast University. Her current research interests include environmental and energy-related catalysis.*

**Yunqian Dai**

*Ping Lu received his Ph.D. in Agricultural and Environmental Chemistry from the University of California Davis. He then worked as a postdoctoral fellow in the Xia group at both Washington University in St. Louis and the Georgia Institute of Technology. He is now an Assistant Professor in the Department of Chemistry and Biochemistry at the Long Island University Brooklyn. His research involves the synthesis, fabrication, and characterization of polymeric and inorganic nanostructures for energy, environmental, and healthcare applications.*

**Ping Lu**

*Zhenming Cao received his B.S. degree in Chemical Engineering and Technology in 2012 from University of Jinan. He is now pursuing his Ph.D. degree with Professor Zhaoxiong Xie at Xiamen University. As a jointly supervised student, he joined the Xia group in November 2017. His research interest is focused on the synthesis of metal nanocrystals for energy-related applications.*

**Zhenming Cao**

*Charles T. Campbell is the Rabinovitch Endowed Chair in Chemistry at the University of Washington. He received his Ph.D. in Physical Chemistry in 1979 with J. M. White from the University of Texas at Austin, and then did postdoctoral research in Germany under Gerhard Ertl (2007 Nobel Prize Winner). He was a staff member at Los Alamos National Lab from 1981-86, then moved to academia. He is an elected Fellow of the ACS, the American Association for the Advancement of Science and the AVS. He served as Editor-in-Chief of Surface Science for over ten years, and now serves as Editor-in-Chief of Surface Science Reports.*

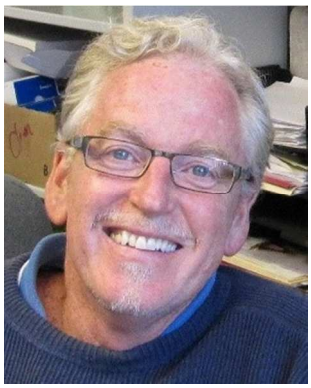

**Charles T. Campbell**

*Younan Xia received his Ph.D. in Physical Chemistry from Harvard University in 1996 with George M. Whitesides. He started as an Assistant Professor of Chemistry at the University of Washington (Seattle) in 1997 and then joined the Department of Biomedical Engineering at Washington University in St. Louis in 2007 as the James M. McKelvey Professor. Since 2012, he has held the position of Brock Family Chair and GRA Eminent Scholar in Nanomedicine at the Georgia Institute of Technology. He has served as an Associate Editor of Nano Letters since 2002.*

**Younan Xia**